

# Water Resources Research



#### RESEARCH ARTICLE

10.1029/2023WR035662

#### **Key Points:**

- Machine learning-based surrogates provide a rapid diagnostic tool to fuse multi-source remotely sensed parameters into land surface models
- Interannual-varying vegetation buffers hydroclimatic variability and redistributes evapotranspiration biotic and abiotic components
- Multi-source remote sensing vegetation products consistently correct the underestimated water yield (as much as 14%) in the UCRB from the static vegetation scheme

#### **Supporting Information:**

Supporting Information may be found in the online version of this article.

#### Correspondence to:

R. Zeng, ruijie.zeng.1@asu.edu

#### Citation:

Longyang, Q., & Zeng, R. (2024). Hydrological impact of remotely sensed interannual vegetation variability in the Upper Colorado River Basin. *Water Resources Research*, 60, e2023WR035662. https://doi.org/10.1029/2023WR035662

Received 27 JUN 2023 Accepted 19 AUG 2024

© 2024. The Author(s).

This is an open access article under the terms of the Creative Commons

Attribution License, which permits use, distribution and reproduction in any medium, provided the original work is properly cited.

## Hydrological Impact of Remotely Sensed Interannual Vegetation Variability in the Upper Colorado River Basin

Qianqiu Longyang<sup>1,2</sup> and Ruijie Zeng<sup>1</sup>

<sup>1</sup>School of Sustainable Engineering and the Built Environment, Arizona State University, Tempe, AZ, USA, <sup>2</sup>Kansas Geological Survey, University of Kansas, Lawrence, KS, USA

**Abstract** Vegetation plays a crucial role in atmosphere-land water and energy exchanges, global carbon cycle and basin water conservation. Land Surface Models (LSMs) typically represent vegetation characteristics by monthly climatological indices. However, static vegetation parameterization does not fully capture timevarying vegetation characteristics, such as responses to climatic fluctuations, long-term trends, and interannual variability. It remains unclear how the interaction between vegetation and climate variability propagates into hydrologic fluxes and water resources. Multi-source satellite data sets may introduce uncertainties and require extensive time for analysis. This study developes a deep learning surrogate for a widely used LSM (i.e., Noah) as a rapid diagnosic tool. The calibrated surrogate quantifies the impacts of time-varying vegetation characteristics from multiple remotely sensed GVF products on the magnitude, seasonality, and biotic and abiotic components of hydrologic fluxes. Using the Upper Colorado River Basin (UCRB) as a test case, we found that time-varying vegetation provides more buffering effect against climate fluctuation than the static vegetation configuration, leading to reduced variability in the abiotic evaporation components (e.g., soil evaporation). In addition, time-varying vegetation from multi-source remote sensing products consistently predicts smaller biotic evaporation components (e.g., transpiration), leading to increased water yield in the UCRB (about 14%) compared to the static vegetation scheme. We also highlight the interaction between dynamic vegetation parameterization and static parameterization (e.g., soil) during calibration. Parameter recalibration and a re-evaluation of certain model assumptions may be required for assessing climate change impacts on vegetation and basin-wide water resources.

#### 1. Introduction

Vegetation plays an important role in terrestrial water and energy budgets (Bonan, 2008; Duveiller et al., 2018; Oehri et al., 2022), global carbon cycle (J. M. Chen, Ju, et al., 2019; Sha et al., 2022) and adaptation to a changing climate (Anderson & Song, 2020; Duarte et al., 2013; Thorne et al., 2017). Vegetation transpiration directly affects terrestrial-atmospheric processes as the main component in latent heat flux, accounting for about 40%-80% of latent heat flux (Coenders-Gerrits et al., 2014; Good et al., 2015; Schlesinger & Jasechko, 2014; L. Wang et al., 2014). In addition, vegetation indirectly interacts with other hydrologic processes in response to climate forcing. For example, hydraulic redistribution through vegetation root systems regulates soil moisture to accommodate climate fluctuation (Amenu & Kumar, 2008; Barron-Gafford et al., 2017; L. Sun et al., 2018; Yu & D'Odorico, 2014). The vegetation shade and canopy snow interception change the land surface albedo and snow energy balance in cold regions (Link & Marks, 1999; Malle et al., 2019; Webster & Jonas, 2018). These feedbacks subsequently propagate to catchment fluxes such as surface water yield, evapotranspiration and groundwater recharge (Vertessy et al., 2001; Wattenbach et al., 2012). Furthermore, the detected alterations in vegetation reflect both natural factors (e.g., wildfire) and human activities (e.g., reforestation and deforestation) (Boulton et al., 2022; C. Chen, Park, et al., 2019; Nobre et al., 2016), which introduce further uncertainty when evaluating the effects of vegetation on the hydrological cycle. Therefore, improving the representation of vegetation dynamics and its interaction with climate forcings and hydrologic processes are essential for predicting hydrologic fluxes and state variables in a changing environment (Kumar et al., 2019; Miller et al., 2006; Ruhge & Barlage, 2011).

Land surface models (LSMs) and hydrologic models typically present plant phenology through static multi-year average monthly climatology. For instance, the Unified Noah LSM (F. Chen & Dudhia, 2001; F. Chen et al., 1996; Ek et al., 2003), a stand-alone, uncoupled, 1-D column LSM used in the North American Land Data Assimilation System Phase 2 (NLDAS-2, Xia et al., 2012), employs the climatological Green Vegetation Fraction

LONGYANG AND ZENG 1 of 23

1944 7973, 2024, 9, Downloaded from https://agupubs.onlinelibrary.wiley.com/doi/10.1029/2023WR035662 by Arizona State University Acq, Wiley Online Library on [04/10/2024]. See the Terms and Conditions (https://onlinelibrary.wiley.

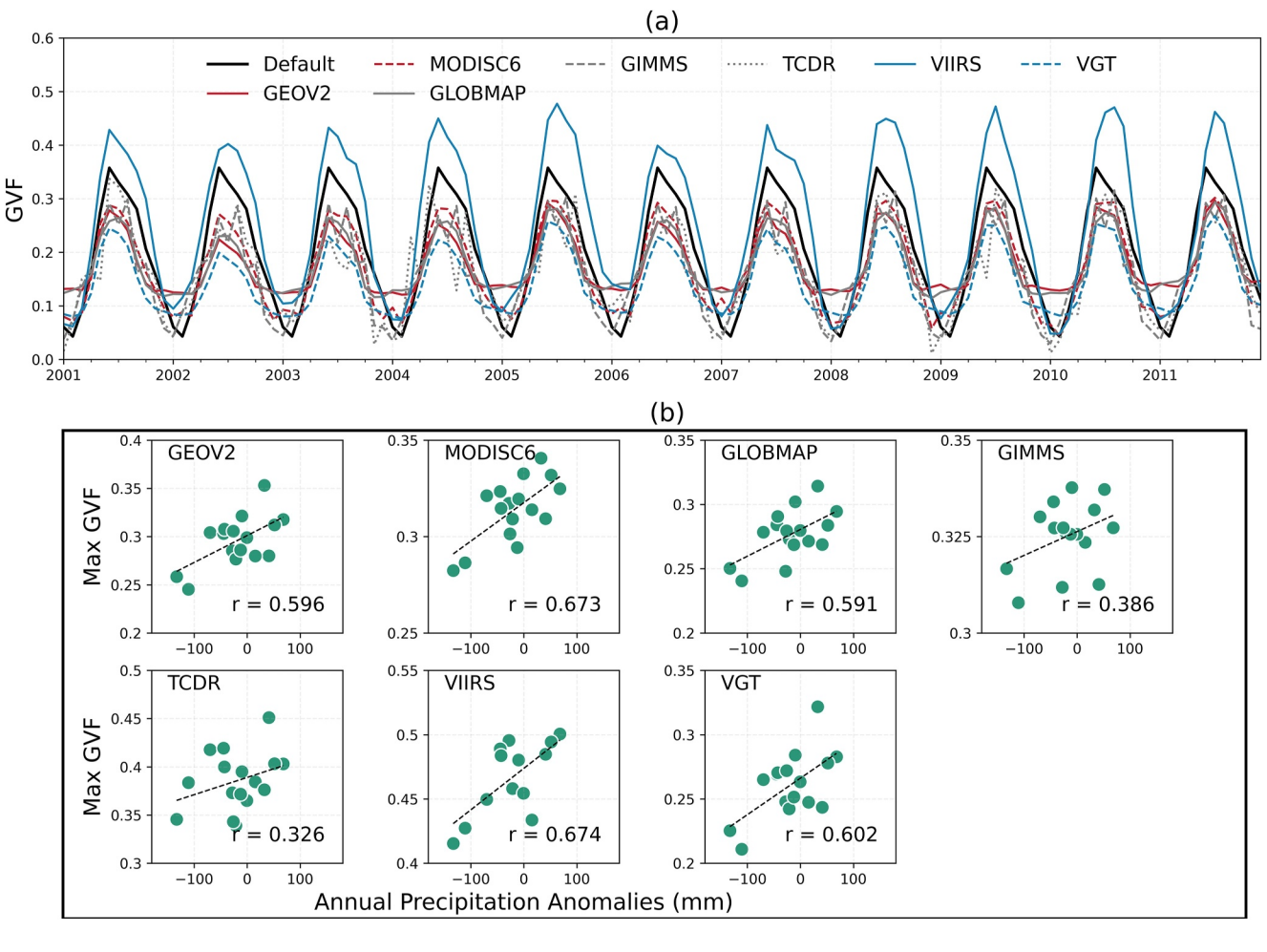


**Figure 1.** (a) Monthly average GVF during the period of 2001–2011 across the Upper Colorado River Basin (UCRB), here "Default" represents the climatological GVF obtained using a composite 5-year (1985–1989) GVF derived from the AVHRR; (b) Correlation between annual maximum GVF from various products (GEOV2, MODIS C6, GLOBMAP, GIMMS, TCDR, VIIRS, and VGT) and annual precipitation. Details of remotely sensed products refer to Table 1.

(GVF, as the black solid line shown in Figure 1a) to parameterize vegetation dynamics using a composite 5-year (1985–1989) average derived from the Advanced Very High Resolution Radiometer (AVHRR) satellite (Gutman & Ignatov, 1998). Such climatology parameterization scheme only represents vegetation average seasonal variation and misses the interannual variability (as colored lines shown in Figure 1a), therefore failing to capture the actual vegetation responses to climate fluctuations and extremes (e.g., droughts) and leading to errors in estimates of the hydrologic fluxes and states (e.g., Q. Tang et al., 2012; Wattenbach et al., 2012).

In semi-arid and arid regions like the Upper Colorado River Basin (UCRB), the structure and distribution of vegetation can be highly regulated by precipitation patterns (Dannenberg et al., 2019; Miranda et al., 2011; Poulter et al., 2014). Figure 1b illustrates the correlation between annual maximum GVF derived from the seven remotely sensed vegetation products and annual precipitation anomalies from the NLDAS-2 forcing. All seven remotely sensed GVFs (details see Table 1) consistently show correlations with annual precipitation, indicating the vegetation response to climatic variability in the semi-arid UCRB. As global warming induces notable increases in atmospheric water demand and vegetation water consumption across diverse regions (Yuan et al., 2019; Y. Zhang, Parazoo, et al., 2020), the association between precipitation and vegetation variability in drylands is expected to be enhanced (Zhao et al., 2022). Furthermore, the mean sensitivity of vegetation canopy greenness to precipitation, as observed from satellites, is highest in arid regions and has been increasing over time in many drylands, including the western U.S., since the 1980s (Y. Zhang et al., 2022). The consistent observational evidence of the interaction between vegetation dynamics and precipitation suggests that the projected variations in precipitation could both directly adjust the water input to the system and alter vegetation indices, thereby

LONGYANG AND ZENG 2 of 23

Table 1
Summary of Remotely Sensed GVF Data Sets Employed in This Study

	Products	Sensor	Spatial resolution	Temporal resolution	Period
LAI-based	GEOV2	SPOT/VGT, MODIS	1 km	10 days	1999-
	MODIS C6	MODIS Terra	500 m	8 days	2000-
	GLOBMAP	AVHRR, MODIS	8 km	Half month (1981–2000); 8-day (2001-present)	1981-
	GIMMS	AVHRR, MODIS, SPOT/VGT	1/12°	15 days	1981-
	TCDR	AVHRR	0.05°	Daily	1981-
Spectral based	VIIRS	VIIRS	1 km	Daily	1981-2012
	VGT	SPOT/VGT, MODIS	1 km	10 days	1999-

introducing additional variance in hydrologic response. As a result, it is crucial to integrate interannually variant vegetation dynamics into LSMs for a more accurate representation of precipitation-vegetation association.

Mechanistic representations involve simulating vegetation dynamics through ecohydrological processes within the LSMs (e.g., dynamic vegetation module in the Noah-Multiparameterization Land Surface Model, Niu et al., 2011). However, dynamic vegetation models are typically limited by simplified process representations and model parameterization uncertainty. Hence, the simulated dynamic phenology can be notably biased (Konings & Gentine, 2017; Murray-Tortarolo et al., 2013) and often fails to reproduce the full extent of observed temporal variability (Kolassa et al., 2020; Koster et al., 2014; Lee et al., 2018).

Remotely sensed time-varying vegetation indices are progressively incorporated into hydrologic models to yield a more accurate estimate of hydrologic states and fluxes. Enhancements in model performance, achieved by replacing the original climatological vegetation parameterization with real-time satellite data sets, are evident in simulated surface soil moisture and temperature (Yin et al., 2016), streamflow predictions (Elmer et al., 2022; T. Ma et al., 2019; Tesemma et al., 2015), and snow depth and terrestrial water storage (Kumar et al., 2019). However, there are concerns associated with incorporating remotely sensed vegetation characteristics into large-scale hydrologic models. Discrepancies among various remotely sensed vegetation data sets can be substantial due to diverse sources of satellite sensors and retrieval algorithms. Although previous studies showed the benefits of fusing one specific vegetation index into hydrologic models, the propagation of uncertainty of multi-source remotely sensed vegetation products through hydrologic processes and impacts on hydrological simulations remains unclear (Cihlar et al., 1997; X. Zhu et al., 2018). Moreover, the incorporation of multi-source remotely sensed data into modeling is a time-consuming process. There is a need for rapid diagnostic tools to aid in the evaluation and selection of appropriate remotely sensed data.

Machine Learning (ML) has gained considerable traction as a method to expedite hydrological simulations in recent years. It learns the relationships between various independent and dependent variables. When the target outputs of the ML models are sourced from process-based models, the ML serves as a surrogate, effectively "replicating" the underlying mechanisms of the physical model. This surrogate role allows them to directly produce target outputs, achieving both high predictive accuracy and reduced computational runtime, as demonstrated in studies by Zahura et al. (2020), Zahura and Goodall (2022), Tran et al. (2021), Maxwell et al. (2021), and Condon et al. (2021). Additionally, ML surrogates facilitate speeding up parameter estimation and uncertainty quantification (R. Sun et al., 2023; Xu et al., 2017), thereby improving the forecasting accuracy and predictive capabilities of hydrological models. Therefore, leveraging the potential of ML is a promising approach for efficiently integrating multi-source remotely sensed data into large-scale hydrologic models.

This study aims to examine the spatiotemporal impacts of fusing multi-source remotely sensed time-varying vegetation dynamics into LSMs on hydrologic simulations in the UCRB. With diverse natural conditions (e.g., climate, seasonality, topography, and vegetation types) and significant societal impacts in a changing environment, the UCRB provides a wide spectrum to comprehensively assess the consequences of vegetation-hydrology interaction and land management. We aim to address the following questions: (a) Can multi-source remotely sensed vegetation products capture the vegetation responses to climatic interannual variability? (b) In the UCRB, what are the hydrologic consequences of explicitly represented time-varying vegetation dynamics? (c) How does the response of vegetation to climatic fluctuation regulate hydrologic biotic and abiotic components, and what are

LONGYANG AND ZENG 3 of 23

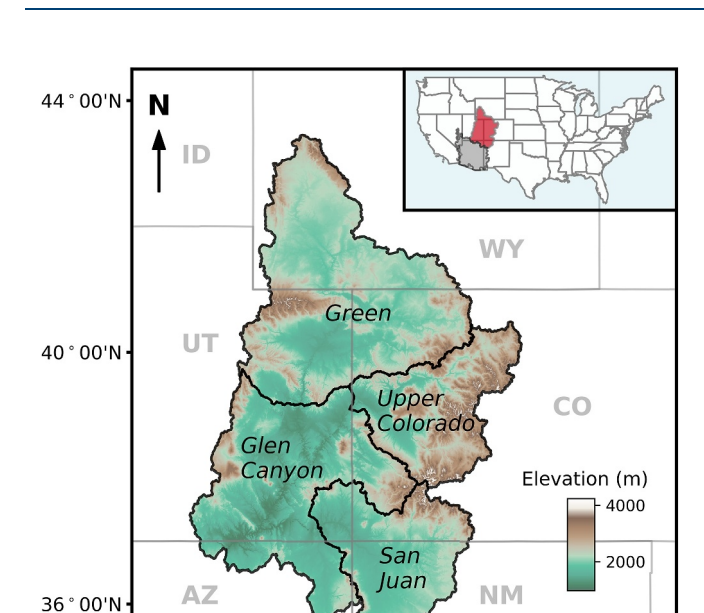


Figure 2. Location of Upper Colorado River Basin (UCRB) and subbasins.

108°00'W

100

112°00'W

200

km د

the implications to water resources in the UCRB? We develop a deep learning-based surrogate model based on the Noah LSM as a computationally efficient diagnostic tool to facilitate the parameter calibration and fusing of remote sensing products and process-based hydrologic models.

### 2. Methods

#### 2.1. Study Area

As a prominent river in the southwestern U.S., the Colorado River spans seven U.S. states and Mexico, catering to the needs of 40 million people and providing irrigation water for 5.5 million acres of agricultural land (Cohen et al., 2013). The natural flow of the Colorado River is heavily influenced by snowpack in the Rocky Mountain headwaters subbasins, accounting for over 70% of the river's annual streamflow (D. Li et al., 2017). The UCRB, which generates approximately 90% flow of the entire Colorado River Basin (CRB) (Jacobs, 2011; McCabe & Wolock, 2020; Xiao et al., 2018), is the primary focus of hydrologists. This snowmelt-dominated catchment extends from the headwaters in the Rockies of Colorado and Wyoming to Lee's Ferry in Northern Arizona, with elevations ranging from approximately 4,300–900 m and covering an area of about 280,000 km² (Tran et al., 2022). The climate of UCRB exhibits considerable variation, transitioning from alpine conditions in the north and east to arid/semi-arid conditions in the south and west (Ficklin et al., 2013). The UCRB experiences an average annual precipitation of

400 mm, predominantly accumulating in mountainous regions (Hibbert, 1979), and ranging from over 1,000 mm in the east to less than 250 mm in the west (Ficklin et al., 2013). Water balance fluctuations in the basin are primarily driven by ET, which constitutes over 85% of precipitation on average (Vano et al., 2012). The basin features a predominance of shrubland and various forest types, together comprising approximately 60% and 25% of the total UCRB land cover, respectively. The UCRB encompasses the Green, Upper Colorado, Glen Canyon, and San Juan River subbasins (Figure 2).

## 2.2. Land Surface Model (LSM)

104°00'W

We select the NLDAS-2 Noah LSM version 2.8 as the focus for diagnostic analysis. The Noah LSM serves as one of the land surface modeling components within the NASA Land Information System (LIS, Kumar et al., 2006), which typically operates in an uncoupled mode, utilizing a combination of observation-based precipitation, radiation, and meteorological and land surface parameter data sets. It is a one-dimensional soil-atmosphere-vegetation transfer model which simulates four-layer soil moisture (both liquid and frozen) with respective thicknesses of 0–0.1, 0.1–0.4, 0.4–1, and 1–2 m (F. Chen & Dudhia, 2001; F. Chen et al., 1996; Ek et al., 2003). Specifically, the Noah model version 2.8 is employed in the NLDAS-2 to generate long-term (1979-present), high-resolution (1/8°) energy and water flux as well as state variables (Kumar et al., 2017; Xia et al., 2012). Although the operational version of NLDAS-2 is expected to undergo subsequent enhancement via its transition to the NLDAS-Testbed at NCEP for future implementation by upgrading and/or replacing old versions and models and adding new assimilation procedures (B. Zhang, Xia, et al., 2020), the diagnostic methodology presented herein remains readily transferable to alternative land surface models driven by NLDAS-2 forcing, and is amenable to applications within the context of other hydrological models.

In this study, particular emphasis is placed on the estimation of ET and its associated subcomponents, which are primarily governed by vegetation dynamics. Within the Noah LSM, the GVF dictates the partitioning of total ET into vegetation transpiration and evaporation originating from both bare soil and vegetative canopy. Additionally, GVF indirectly influences the snow sublimation rate by modulating state variables implicated in the water balance. In the following part of this section, we briefly introduce the processes affected by vegetation in Noah LSM, while a comprehensive description of Noah LSM can be found in F. Chen and Dudhia (2001). The total ET consists of four components, the direct evaporation  $E_{\rm dir}$ , the wet canopy evaporation  $E_c$ , the canopy evaporation  $E_t$  and the snow sublimation,  $E_{\rm sn}$ , namely,

LONGYANG AND ZENG 4 of 23

$$ET = E_{dir} + E_c + E_t + E_{sn}$$
 (1)

Specifically, the direct evaporation  $E_{\text{dir}}$  from the ground surface is computed by

$$E_{\text{dir}} = (1 - \sigma_f)\beta \cdot E_p \tag{2}$$

where  $E_p$  is the potential evaporation calculated by a Penman-based energy balance approach that includes a stability-dependent aerodynamic resistance (Mahrt & Ek, 1984),  $\beta$  is the first layer's soil moisture normalized by the field capacity and wilting point, and  $\sigma_f$  is the GVF.

The wet canopy evaporation  $E_c$  is determined by

$$E_c = \sigma_f \left(\frac{W_c}{S}\right)^n \cdot E_p \tag{3}$$

where  $W_c$  is the intercepted canopy water content, S is the maximum canopy capacity, and n = 0.5.

The plant transpiration  $E_t$  is determined by

$$E_t = \sigma_f B_c \left[ 1 - \left( \frac{W_c}{S} \right)^n \right] \cdot E_p \tag{4}$$

where  $B_c$  is a function of canopy resistance and is formulated as

$$B_c = \frac{1 + \frac{\Delta}{R_r}}{1 + R_c C_h + \frac{\Delta}{R_r}} \tag{5}$$

where  $C_h$  is the surface exchange coefficient for heat and moisture;  $\Delta$  depends on the slope of the saturation specific humidity curve;  $R_r$  is a function of surface air temperature, surface pressure, and  $C_h$ ; and  $R_c$  is the canopy resistance determined by

$$R_c = \frac{R_{\text{cmin}}}{\text{LAI} \cdot F_1 F_2 F_3 F_4 \cdot s} \tag{6}$$

$$F_1 = \frac{R_{\text{cmin}}}{1+f} + f \text{ where } f = 0.55 \frac{R_g}{R_{vl}} \frac{2}{\text{LAI}}$$
 (7)

where  $F_1$ ,  $F_2$ ,  $F_3$ , and  $F_4$  represent the effects of solar radiation, vapor pressure deficit, air temperature, and soil moisture, respectively; s is the seasonal factor, determined by the optimum root growth temperature and mean soil temperature over the root zone;  $R_g$  is the incoming solar radiation, and  $R_{g1}$  is a lower limit of 30 W·m<sup>-2</sup> for forests and 100 W·m<sup>-2</sup> for crops (Noilhan & Planton, 1989);  $R_{cmin}$  is the minimum stomatal resistance;  $R_{cmax}$  is the cuticular resistance of the leaves. LAI is the leaf area index, and the calculation of seasonal LAI in Noah LSM is altered to depend on the vegetation class, rewritten as

$$LAI = LAI_{min} + \alpha(LAI_{max} - LAI_{min})$$
(8)

where  $\alpha = \frac{\sigma_f - \sigma_f}{\sigma_f \max}$  is normalized monthly GVF,  $\sigma_f$  is monthly GVF, and  $\sigma_{fmax}$  and  $\sigma_{fmin}$  are the maximum and minimum GVF, respectively. Table S2 in Supporting Information S1 provides the details of vegetation type-dependent maximum and minimum LAI. More detailed descriptions can be found in the work of Wei et al. (2012).

As the calculation of  $E_{\rm sn}$  does not directly involve GVF, the details are not included here. For more comprehensive information, please refer to Livneh et al. (2010). To summarize, GVF affects ET fluxes in Noah LSM by determining the partitioning of latent heat between vegetation and soil, and further modulating vegetation transpiration by shaping canopy resistance.

LONGYANG AND ZENG 5 of 23

1944/973, 2024, 9, Downloaded from https://agupubs.onlinelibrary.wiley.com/doi/10.1029/2023WR035662 by Arizona State University Acq, Wiley Online Library on [04/10/2024]. See the Term

**Figure 3.** Flowchart summarizing the process for surrogate model construction. The meteorological forcing includes Accumulated hourly precipitation (P), Air temperature (Tair), Specific humidity at 2 m above the surface (Qair), Surface pressure (PSurf), Surface downward longwave radiation (LWDown), Surface downward shortwave radiation (SWDown), U wind component (U wind), V wind component (V wind). The physical parameters (vegetation and soil-related) include GVF, Minimum stomatal resistance (RSMIN), Roughness length (Z0), Parameter used in solar radiation term of canopy resistance function (RGL), Saturated hydraulic conductivity (SATDK), Saturated soil potential (SATPSI), Porosity (MAXSMC), Soil type "B" parameter (BEXP). The output variables include Total runoff (Q), Vegetation transpiration (TRANS), Bare soil evaporation (EVBS), Canopy water evaporation (EVCW), and Snow sublimation (SBSNO).

#### 2.3. Deep Learning-Based Surrogate Model

We develop a surrogate model to streamline the calibration of the Noah LSM (as shown in the flowchart in Figure 3), followed by a diagnostic analysis by fusing multi-source remotely sensed vegetation products into the calibrated surrogate. Surrogate modeling, or emulation, aims to provide a simplified and expedited model that reproduces the specific output of a complex model based on its inputs and parameters (Asher et al., 2015).

#### 2.3.1. Parameter Space and Process-Based Model Running

A high-fidelity surrogate model needs careful sampling to ensure that the surrogate can generalize well over the entire input space without overfitting to particular subsets of the data. This study mainly focuses on the model's generalizability across the parameter space to avoid any unreasonable extrapolation during the parameter calibration process.

We empirically identify key parameters that influence the processes of energy partitioning and runoff generation. The minimum stomatal resistance ( $R_{cmin}$ ) and the parameter used in the solar radiation term of the canopy resistance function ( $R_{gl}$ ) (Equation 7) are also utilized as inputs. These parameters play crucial roles in determining canopy resistance, subsequently influencing the calculation of transpiration. Soil-related parameters fed into the model include saturated hydraulic conductivity, saturated soil potential, porosity, and the soil type "B" parameter. These factors are essential to compute the time rate of change of soil moisture and temperature.

We employ Latin Hypercube Sampling (LHS) to systematically select 1,000 parameter sets within the defined parameter space, following the NLDAS-2 specifications for soil and vegetation parameters (see Table S1 in Supporting Information S1 for details). H. Wang et al. (2023) suggest that the surrogate model is suitable for parameter optimization when the size of the parameter samples is approximately 40 times the number of parameters. LHS can ensure that the surrogate model encompasses a full range of possible parameter values.

For all 1,000 parameter sets, we run the Noah LSM driven by hourly NLDAS-2 meteorological forcing across the entire study area (more than 2,000 grid cells) to produce corresponding outputs of hydrological fluxes, including total runoff (Q, the sum of surface runoff and subsurface runoff) and four subcomponents of ET: transpiration (TRANS), canopy water evaporation (EVCW), bare soil evaporation (EVBS), and snow sublimation (SBSNO). Following Rodell et al. (2005), we initialize the four soil layers of the Noah LSM model at 30% saturation and set them to the multi-year average soil temperature. The model is run for the first 10 water years (1979–1989), and

LONGYANG AND ZENG 6 of 23

this process is repeated 5 times. The model states at the end of the fifth run, specifically on 30 September 1979, are then used as the initial conditions for subsequent simulations. These outputs aggregated from an hourly to a daily scale serve as target variables for the surrogate model construction. This process generates more than 2,000,000 time series for each output variable.

#### 2.3.2. Surrogate Model Configuration

The surrogate model for the Noah LSM is established using Long Short-Term Memory (LSTM, Hochreiter & Schmidhuber, 1997), a deep learning technique adept at capturing temporal dependencies and extensively employed in hydrology in recent years (Feng et al., 2020; Kratzert et al., 2018, 2019; K. Ma et al., 2021). LSTM is designed to capture both short- and long-term dependencies by the use of cell memory in its architecture and is frequently utilized to simulate hydrological fluxes (e.g., ET, Babaeian et al., 2022; Jia et al., 2023) and hydrological states (e.g., soil moisture, Q. Li et al., 2022; Orth, 2021; SWE, short for Snow Water Equivalent, Meyal et al., 2020, Song et al., 2023). A detailed description of the LSTM architecture can be found in Appendix A.

We build a single-layer sequence-to-sequence LSTM model with 256 hidden units to simulate hydrologic fluxes, which processes each input sequence step-by-step (i.e., daily) to generate the corresponding output sequence. Specifically, the LSTM-based surrogate model in this study is implemented to mimic the underlying mechanism of a hydrologic model in a similar manner:

Hydrologic Model: 
$$y_t = f_{\text{Noah}}(x_t, s_{t-1}, \phi)$$
 (9)

Surrogate Model: 
$$\hat{\mathbf{y}}_t = f_{\text{LSTM}}(\mathbf{x}_t, \mathbf{s}_{t-1}, \boldsymbol{\phi}; \boldsymbol{\theta})$$
 (10)

where  $x_t$  is the meteorological forcing at the time step t,  $s_{t-1}$  is the hydrologic states (e.g., soil moisture, snow water equivalent) or LSTM internal states (i.e., hidden state  $h_t$  and cell memory  $c_t$ ) at the previous time step,  $\phi$  is the physical parameters (soil and vegetation-related) in the Noah LSM, and  $\theta$  represents weights and biases of the LSTM-based surrogate model,  $y_t$  is a subcomponent ET or runoff estimation of Noah LSM at the time step t,  $\hat{y}_t$  is the subcomponent ET (i.e., TRANS, EVCW, EVBS, or SBSNO) or total runoff simulated by LSTM at the time step t.

For the surrogate model, the inputs are meteorological forcing and parameter sets, while the outputs are hydrologic fluxes. Model inputs are normalized to a range of 0–1, to ensure faster convergence during the training process. Meteorological forcing data spanning from 1 October 1979 to 30 September 2016, is aggregated from an hourly to a daily scale. The fully connected operator (see Appendix A) enables the LSTM model to learn sufficient interactions between meteorological forcing and physical parameters (e.g., GVF).

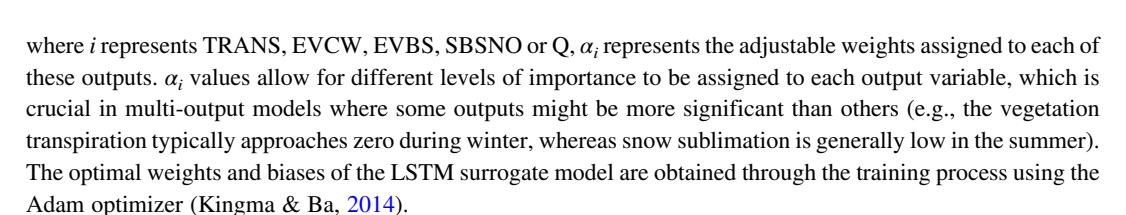
It is crucial to properly initialize the states of an LSTM model in a sequence-to-sequence configuration. Typically, the LSTM's hidden states ( $h_0$ ) and cell memory ( $c_0$ ) are initialized to zero. These states ( $h_t$  and  $c_t$ ) are updated at each timestep, sequentially carrying forward information to generate outputs such as simulated Q and all ET subcomponents. Analogous to the process-based model, this process spans the entire period from 1 October 1979, to 30 September 2016, generating the corresponding output time series. To mitigate initial inaccuracies due to zero-initialized states, the LSTM surrogate model undergoes a "spin-up" period. Initially, the model is run for the first 10 water years (1979–1989), with hidden states set to zero. This process is repeated 5 times. The hidden states on 30 September 1989, after the fifth run, are then used as initial conditions for subsequent simulations. This approach helps stabilize the model's output predictions.

#### 2.3.3. Data Split, Model Training, and Performance Evaluation

The objective function seeks to minimize the Mean Square Error (MSE) of all selected outputs (Q, TRANS, EVCW, EVBS, SBSNO) for both the LSTM surrogate model and the Noah LSM. Specifically, the objective function at each time step *t* is expressed as

$$\min_{\boldsymbol{\theta}} \alpha_i \sum_{j}^{5} \left( \mathbf{y}_{i,t} - \hat{\mathbf{y}}_{i,t} \right)^2 \tag{11}$$

LONGYANG AND ZENG 7 of 23



Since this study mainly focuses on the model's generalizability across the parameter space, for each grid cell, we split the 1,000 parameter sets as follows: 50% of the parameter sets are randomly selected for training, 10% for validation, and the remaining 40% for testing. This split is applied to each grid cell independently, and the combined data from all grid cells is used for the respective training, validation, and testing phases. By using all grid cells (over 2,000 across the entire basin), we aim to ensure the surrogate model can cover the full range of meteorological conditions.

In the training of our model, we employ a strategic learning rate schedule for optimization. For the first 100 epochs, we set the learning rate at  $10^{-3}$  with a mini-batch size of 256 to facilitate rapid convergence. For the following 500 epochs, the learning rate is reduced to  $10^{-4}$ , aiding in more precise adjustments in the model weights. According to the first 100 epochs' performance, we adjust the weights  $\alpha_i$  in Equation 11 from a uniform set (where each weight is initially 1) to varied values through a trial-and-error method for optimal tuning. We further decrease the learning rate to  $10^{-5}$  to refine the model further. During this refining phase, we implement an early stopping mechanism. This approach monitors the model's performance on a validation set and halts the training process if there is no improvement, effectively mitigating the risk of overfitting.

Once the model is well-trained, it is re-run using the parameter sets in the test set (400 time series for each output variable within each grid cell) across the entire basin from 1 October 1979 to 30 September 2016 to assess its performance. The model performance is evaluated using the Nash-Sutcliffe Efficiency (NSE, Nash & Sutcliffe, 1970), Root Mean Square Error (RMSE), and Percent Bias (PBIAS) (formulas provided in Appendix A2). Results under five different random seed settings are evaluated to mitigate uncertainty arising from model implementation (random sampling and weights initialization).

#### 2.3.4. Parameter Calibration

Utilizing the well-trained surrogate model, we implement a Genetic Algorithm (GA) for effective parameter calibration. We aim to determine an optimal set of soil-related physical parameters (specifically, SATDK, SATPSI, MAXSMC, and BEXP) to minimize the MSE between the simulated streamflow and the observed monthly streamflow data at Lee's Ferry, provided by the United States Bureau of Reclamation (USBR) naturalized flow records. To calculate the simulated monthly streamflow, the daily runoff outputs from the surrogate model are aggregated to a monthly scale and then summed across the entire basin, under the assumption that routing process impacts are negligible on this timescale. The GA systematically navigates through the parameter space (parameter range details in Table S1 of Supporting Information S1), in search of the optimal parameter set. In the GA configuration, we specify a population size of 300 with a maximum of 500 generations, a crossover probability of 0.8, and a mutation rate of 0.02. The selection process is based on roulette wheel selection.

The optimal parameter sets calibrated using the GA are then applied to the Noah LSM. Subsequent analysis is conducted utilizing this calibrated model. We further validate the calibrated surrogate model by comparing its outputs with those of the process-based Noah LSM, both using the same set of calibrated soil-related parameters. If the surrogate model can reliably replicate the Noah LSM, the static GVF can be directly replaced with an interannually variant remotely sensed GVF data set during data fusing in the calibrated surrogate.

#### 2.4. Remotely Sensed Green Vegetation Fraction (GVF) Data Set

In order to evaluate the spatial and temporal impact of timing-varying vegetation dynamics on hydrologic simulations within the Noah LSM, several remotely sensed GVF data sets are fused into the well-trained surrogate model. This study employs both LAI-based and spectral-based satellite GVF products. Table 1 provides a summary of the data sources and resolutions for all seven products. LAI-based GVF data sets are derived from Système Probatoire d'Observation de la Terre VEGETATION (SPOT/VGT) Collection Version 2 (hereafter referred to as GEOV2, Verger et al., 2013, 2014), Moderate Resolution Imaging Spectroradiometer Collection 6

LONGYANG AND ZENG 8 of 23

(MODIS C6, Yan et al., 2016), Long-term Global Mapping (GLOBMAP, Y. Liu et al., 2012), Global Inventory Monitoring and Modeling System LAI3g (GIMMS, Z. Zhu et al., 2013), and Terrestrial Climate Data Record (TCDR, Claverie et al., 2016) LAI products. These data sets are converted using the following equation, in accordance with Norman's method (Norman et al., 1995):

$$GVF = 1 - e^{b \times LAI} \tag{12}$$

where b = 0.5 is the extinction coefficient for general plant canopy.

The Visible Infrared Imager Radiometer Suite (VIIRS, Jiang et al., 2016) and SPOT/VGT Collection Version 2 (herein VGT, Verger et al., 2013, 2014) GVF data sets are derived from the presumed linear relationship between GVF and the Normalized Difference Vegetation Index (NDVI) or the Enhanced Vegetation Index (EVI).

All raw LAI or GVF tiles are post-processed including smoothing, gap-filling, and mosaicking to generate global maps at their original spatial resolution, which are subsequently aggregated to an average resolution of 1/8°. Monthly GVF fields are considered valid for the 15th day of each month. The study covers the common periods of all data products from the calendar years 2001-2011. The black solid line in Figure 1a represents the multi-year average monthly climatological GVF parameterization adopted by NLDAS-2 Noah LSM, which is a composite of a 5-year (1985-1989) GVF data set using the AVHRR satellite, based on the algorithm by Gutman and Ignatov (1998). Most of the processed interannually variant GVF products (colored lines, referred to as "dynamic GVF") are smaller than the default climatological GVF (referred to as "static GVF") during the growing seasons, but larger during the winter months (Figure 1a). Despite the differences in algorithms and original spatial and temporal resolutions, dynamic GVFs exhibit consistently similar seasonal patterns and temporal trends, except for VIIRS. This consistency is likely due to the fact that most vegetation indices are fused with other products. During the growing season, the domain average VIIRS GVF is noticeably higher than the static GVF and other dynamic GVF products. VIIRS channels have higher spectral and spatial resolution than AVHRR bands (Elmer et al., 2022), potentially indicating a better representation of vegetation canopies and canopy gaps, partially due to improved observation in high biomass regions with no apparent saturation in forested areas, reduced bidirectional reflectance distribution function effects, and decreased atmospheric influences (Ding & Zhu, 2018). In the following analyses, we will also place particular emphasis on VIIRS, in addition to discussing the median statistics of the impact of all remote sensing products.

#### 3. Results

#### 3.1. Validation of Deep Learning-Based Surrogate Model

The total runoff and ET subcomponents generated by the LSTM surrogate model show a great agreement with the Noah LSM simulations. The NSE values for total runoff (Q), total ET, TRANS, EVCW, EVBS, and SBSNO are 0.9914, 0.9943, 0.9971, 0.9973, 0.9963, and 0.9910, respectively. The RMSE values for all outputs remain below 0.15 mm/day, while the PBIAS values are within a range of  $\pm 2\%$ . Here the total runoff (Q) and subcomponents of ET are directly obtained from the surrogate model output, while total ET is calculated as the sum of all the individual components. The LSTM emulation accuracy is deemed acceptable, exhibiting a promising capability to capture main hydrologic flux variables under the given meteorological forcing and hydrologic parameter sets.

We then run the process-based model and the LSTM surrogate using the calibrated soil-related parameters and compare their respective outputs. The calibrated model demonstrates good performance when compared to the USBR naturalized streamflow estimate in Lee's Ferry (see Figure S1 in Supporting Information S1). It reproduces the overall seasonal trends and regional attributes of total runoff (Q) and ET components throughout the UCRB (Figures S1 and S2 in Supporting Information S1). The surrogate accurately emulates the bi-modal pattern of total ET, which mainly stems from that of bare soil evaporation. The simulation bias of snow sublimation may imply that the surrogate model has limited representations of snow processes in the Noah LSM (Figure 4f). This limitation could potentially impair the total runoff simulation of the surrogate model, considering the substantial contribution of snow-covered regions to the entire basin's water yield and the complicated snow processes involved in its runoff generation. While the surrogate model effectively tracks the increasing runoff from winter to spring and the subsequent decline through summer and fall for all four subbasins, it tends to slightly underestimate Q (Figure 4a and Figure S1 in Supporting Information S1). Despite these minor discrepancies, the LSTM

LONGYANG AND ZENG 9 of 23

1944 7973, 2024, 9, Downloaded from https://agupubs.onlinelibrary.wiley.com/doi/10.1029/2032WR035662 by Arizona State University Acq, Wiley Online Library on [04/10/2024]. See the Terms and Conditions (https://onlinelibrary.wiley.com/doi/10.1029/2032WR035662 by Arizona State University Acq, Wiley Online Library on [04/10/2024]. See the Terms and Conditions (https://onlinelibrary.wiley.com/doi/10.1029/2032WR035662 by Arizona State University Acq, Wiley Online Library on [04/10/2024]. See the Terms and Conditions (https://onlinelibrary.wiley.com/doi/10.1029/2032WR035662 by Arizona State University Acq, Wiley Online Library on [04/10/2024]. See the Terms and Conditions (https://onlinelibrary.wiley.com/doi/10.1029/2032WR035662 by Arizona State University Acq, Wiley Online Library on [04/10/2024]. See the Terms and Conditions (https://onlinelibrary.wiley.com/doi/10.1029/2032WR035662 by Arizona State University Acq, Wiley Online Library on [04/10/2024]. See the Terms and Conditions (https://onlinelibrary.wiley.com/doi/10.1029/2032WR035662 by Arizona State University Acq, Wiley Online Library on [04/10/2024]. See the Terms and Conditions (https://onlinelibrary.wiley.com/doi/10.1029/2032WR035662 by Arizona State University Acq, Wiley Online Library on [04/10/2024]. See the Terms and Conditions (https://onlinelibrary.wiley.com/doi/10.1029/2032WR035662 by Arizona State University Acq, Wiley Online Library on [04/10/2024]. See the Terms and Conditions (https://onlinelibrary.wiley.com/doi/10.1029/2032WR035662 by Arizona State University Acq, Wiley Online Library on [04/10/2024]. See the Terms and Conditions (https://onlinelibrary.wiley.com/doi/10.1029/2032WR035662 by Arizona State University Acq, Wiley Online Library on [04/10/2024]. See the Terms and Conditions (https://onlinelibrary.wiley.com/doi/10.1029/2032WR035662 by Arizona State University Acq, Wiley Online Library on [04/10/2024]. See the Terms and Conditions (https://onlinelibrary.wiley.com/doi/10.1029/2032WR035662 by Arizona State University Acq, Wiley Online Lib

nditions) on Wiley Online Library for rules

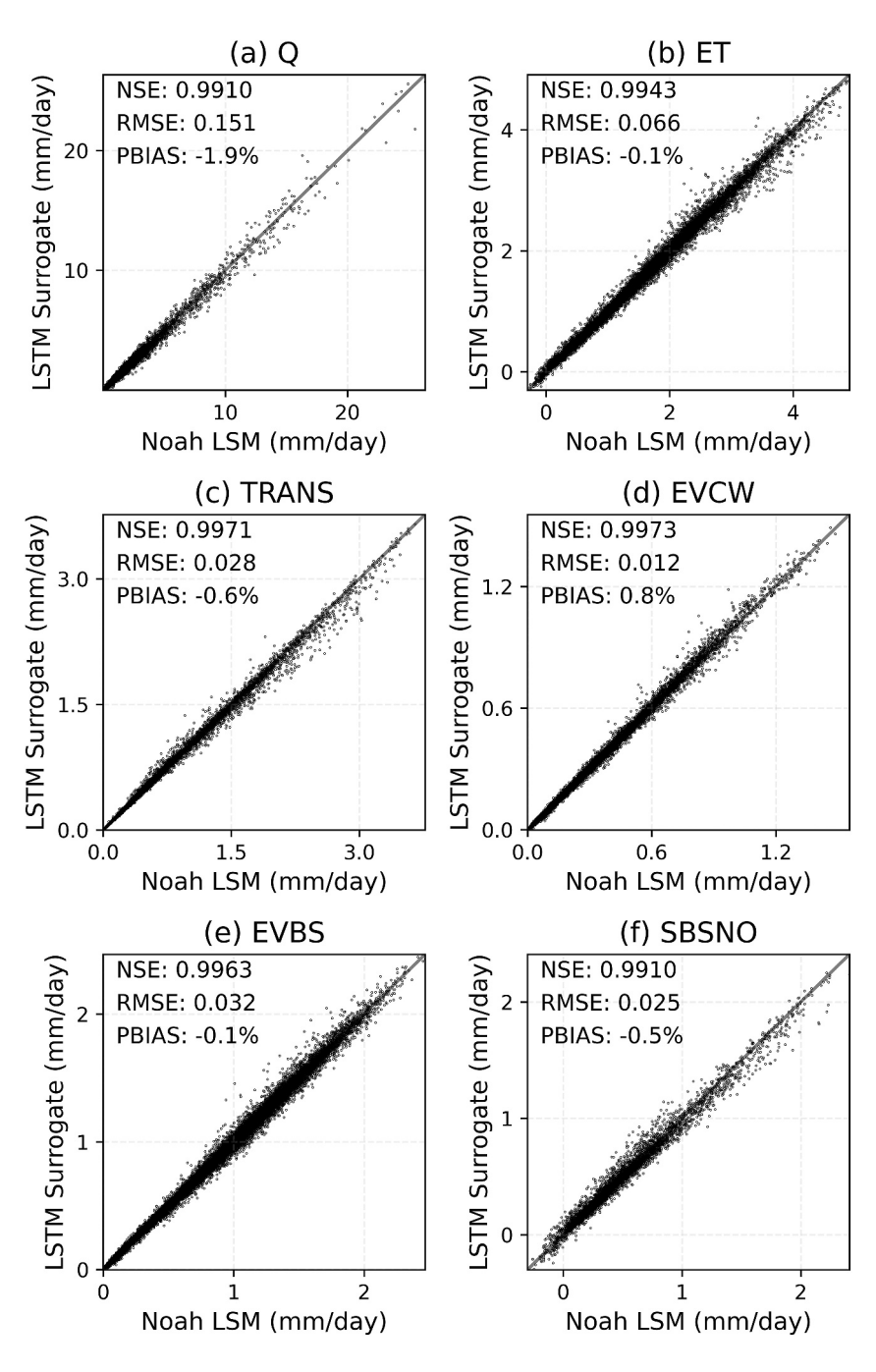


**Figure 4.** Performances of LSTM Surrogate Model for All Selected Target Outputs, including (a) total runoff (Q), (b) total ET, (c) transpiration (TRANS), (d) canopy water evaporation (EVCW), (e) bare soil evaporation (EVBS) and (f) snow sublimation (SBSNO).

surrogate model demonstrates a strong performance in simulating the temporal dynamics of ET and Q across the UCRB. After the integration of the remotely sensed GVF, the calibrated surrogate model continues to exhibit a high level of agreement with the outputs from the calibrated Noah LSM at the daily scale (Figure S3 in Supporting Information S1). This indicates that the surrogate model maintains reasonable extrapolation accuracy, even with the introduction of dynamic GVF data. Therefore, the subsequent analysis conducted using the LSTM surrogate model can be considered reliable.

LONGYANG AND ZENG 10 of 23

19447973, 2024. 9, Downloaded from https://agupubs.onlinelibrary.wiley.com/doi/10.1029/2023WR035662 by Arizona State University Acq, Wiley Online Library on [04/10/2024]. See the Terms and Condit

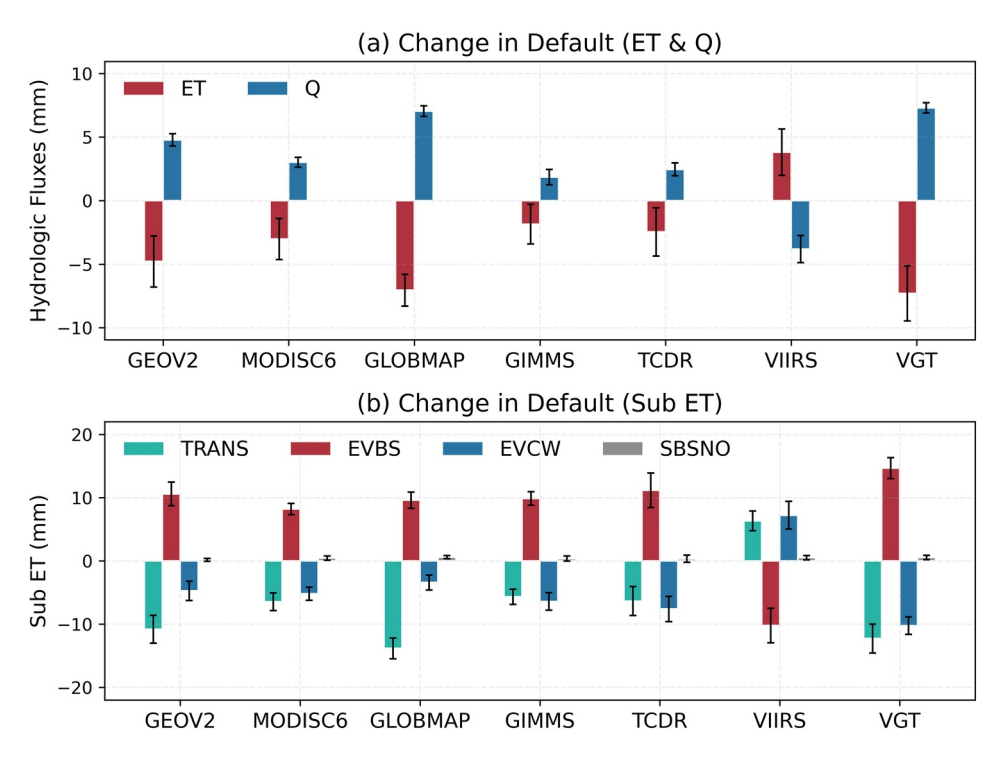


Figure 5. (a) Changes in mean annual ET and runoff (Q) in the UCRB after the integration of satellite-derived interannually varying GVF Products into the Noah LSM compared to that with static parameterization (i.e., default climatological GVF); (b) Analogous to panel (a), but for subcomponents of ET, including transpiration (TRANS), bare soil evaporation (EVBS), canopy water evaporation (EVCW), and snow sublimation (SBSNO). The color-coded bars represent the multi-year average values, while the black error bars indicate the standard deviations for the period 2001–2011.

#### 3.2. Effects of Incorporating Remotely Sensed Vegetation Dynamics Into LSM

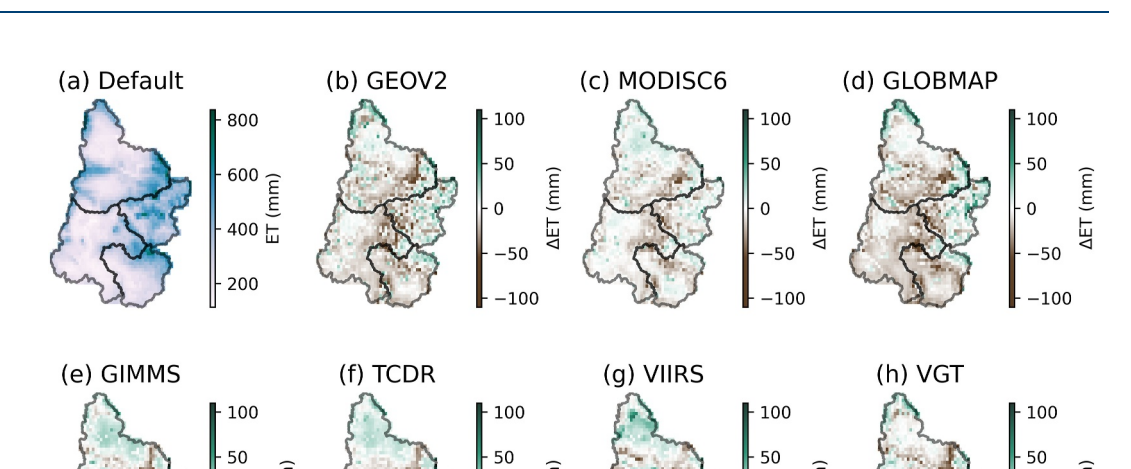
#### 3.2.1. Impacts of Interannually Variant Vegetation Dynamics on Basin-Wide Water Budget

Figure 5 presents a comparison of differences in total runoff (Q), total ET, and its four components (TRANS, EVBS, EVCW, and SBSNO) before and after incorporating year-to-year variable remotely sensed GVF data sets in the UCRB during the 2001–2011 period. While remotely sensed GVF products differ in the interannual variability (Figure S9 in Supporting Information S1), most products (except VIIRS) consistently yield higher mean annual total runoff, ranging from +2.46 to +7.30 mm compared to Noah LSM with static vegetation parameterization (i.e., default climatological GVF). Although the differences in total Q magnitude are less than 10 mm basin-wise, it accounts for around 14% change relative to the multi-year average total Q of 56 mm in the UCRB during 2001–2011. The VIIRS results in a small decrease in total Q estimation (–3.81 mm). The two processed near-real-time GVF data sets from the same source, GEOV2 and VGT, exhibit a similar degree of increase in total Q after data fusion for 2001–2011, despite the former being LAI-based and the latter being spectral-based. The differences in total ET estimation after data fusion between GEOV2 and VGT may reflect the influence of GVF derivation methods (biomass or spectral) on hydrologic simulations in the UCRB.

For all satellite products, changes in total ET lead to nearly equivalent and opposite changes in Q in Figure 5a. This further indicates the LSTM surrogate model conserves the water balance at a long-term scale. Although other hydrologic variables are not simulated by the surrogate model, it is expected that ET changes caused by dynamic vegetation characteristics will lead to changes in other processes. For example, the sensible heat or land surface temperature during the growing seasons is expected to decrease based on energy balance.

Figure 5b further shows the differences in various ET components caused by dynamic GVF parameterization. The satellite-based GVF consistently shows larger bare soil evaporation than default monthly climatological parameterization (varying from 7 to 15 mm; except for VIIRS), which is partially compensated by decreased transpiration and canopy water evaporation. It may be attributed to lower GVF values from remote sensing during growing seasons than Noah's static parameterization. LSM model configurations (Equation 2) indicate that this

LONGYANG AND ZENG 11 of 23



**Figure 6.** Spatial patterns of multi-year average (2001–2011) annual total ET across the UCRB for (a) Default, (b) GEOV2—Default, (c) MODISC6—Default, (d) GLOBMAP—Default, (e) GIMMS—Default, (f) TCDR—Default, (g) VIIRS—Default, (h) VGT - Default.

smaller GVF leads to larger bare soil exposure, resulting in a substantial increase in bare soil evaporation among the four ET subcomponents. Upon integrating VIIRS, which presents higher GVF values during the growing season, bare soil evaporation experiences a decline. Nevertheless, the concurrent rise in transpiration and canopy water evaporation compensates for this decrease, leading to a minor increase in total ET (Figure 5a). Alterations in snow sublimation after fusing remote sensing products with interannual GVF variability are negligible. It may stem from GVF's indirect impact on snow sublimation within the Noah LSM.

Alterations in water budget terms induced by dynamic vegetation parameterization show inconsistent spatial patterns among different satellite products (Figure 6). In high-altitude regions in the Upper Colorado featuring woodland, wooded grassland, and evergreen needleleaf forest, the incorporation of remotely sensed GVF commonly triggers a positive change in annual total ET compared with Noah LSM employing monthly climatological GVF (except VIIRS). In the case of GEOV2, GLOBMAP, and VGT, the decrease in ET largely concentrates in shrubland regions within the southern UCRB. VIIRS GVF in the southern subbasins manifests an early onset and extended duration of greenness (Figure S4 in Supporting Information S1), notably in San Juan. This leads to an elevated total ET estimate and a corresponding decrease in total runoff (Figure S7 in Supporting Information S1). Such spatial variations emphasize the diverse response of remote sensing products to vegetation types, a discrepancy that can propagate into hydrological flux estimates.

The impacts of dynamic vegetation on the interannual variability, indicated by the coefficient of variation (CV), of the annual total ET, vegetation transpiration, bare soil evaporation, and snow sublimation across the UCRB is shown in Figure 7 (GEOV2 as an example, the details of all products see Figure S9 in Supporting Information S1). While the integration of various remotely sensed GVF data sets into Noah LSM leads to slight changes in the water budget terms averaged across the entire basin, they substantially influence the interannual variability of hydrologic fluxes over space. For GEOV2, in most regions except the northern Green and high-altitude regions in the Upper Colorado, satellite-derived dynamic vegetation characteristics increase the interannual variability of total ET and reduce that of total Q. The increased interannual variability in total ET mainly comes from the biotic subcomponents, with increased variability in vegetation transpiration and canopy water evaporation likely mirroring the actual response of vegetation (as captured in remotely sensed GVF products) to climate fluctuations. The reduction in interannual variability of bare soil evaporation across most regions indicates that the surface soil moisture can be more stable year by year. It can be attributed to dynamic vegetation characteristics that buffer (or exhibit resilience against) fluctuations in hydrologic fluxes and states. This highlights the ability of remotely sensed GVF products in capturing physiologic buffering effects against climate variability. The role of vegetation as a climate buffer highlights the importance of updating time-varying vegetation information in LSM simulations to better represent the hydrological variability.

LONGYANG AND ZENG 12 of 23

1944 7973, 2024, 9, Downloaded from https://agupubs.onlinelibrary.wiely.com/doi/10.1092/023WR035662 by Arizona State University Acq, Wiley Online Library on [04/10/2024]. See the Terms and Conditions (https://onlinelibrary.wiely.com/terms/

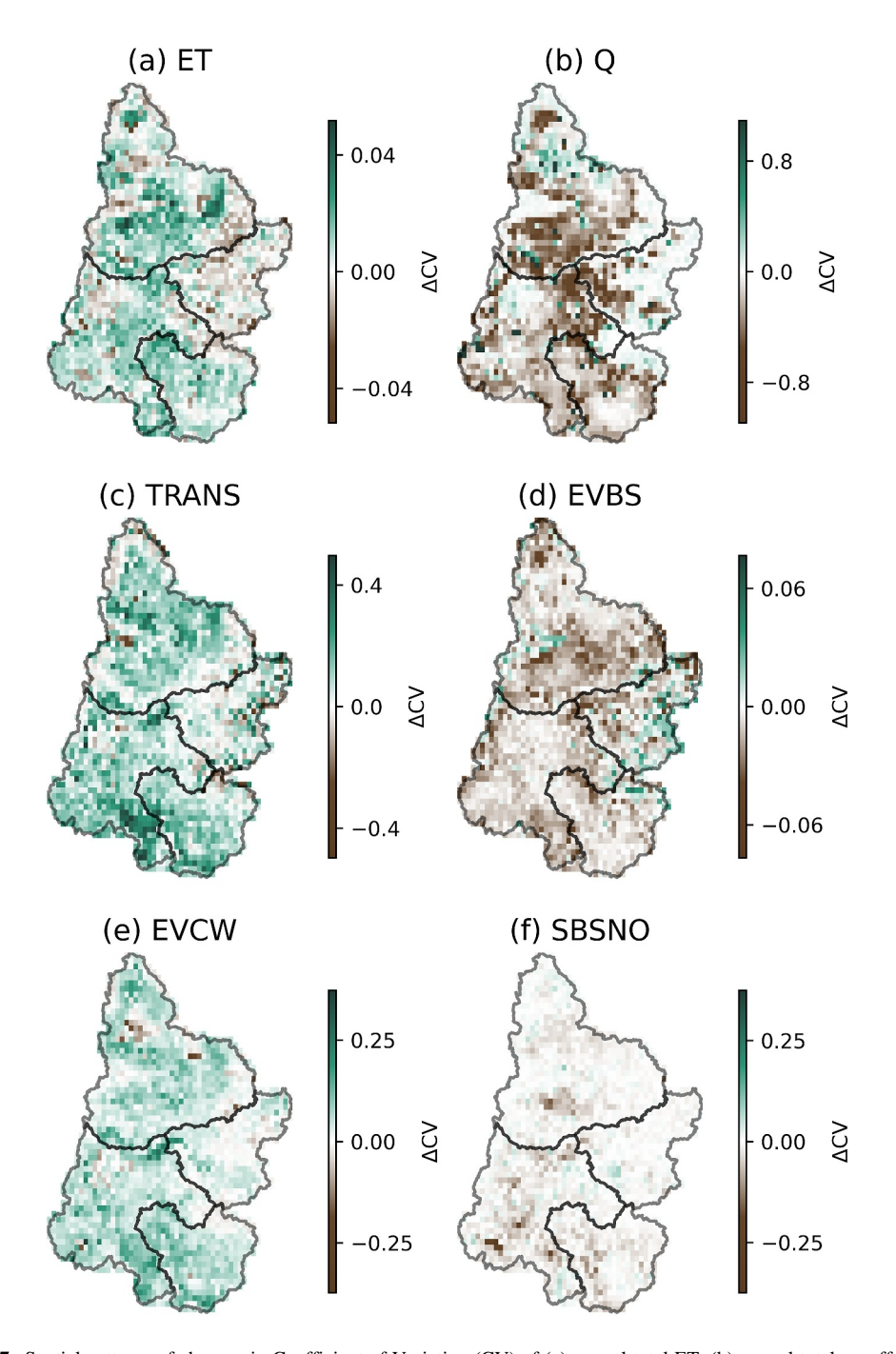


**Figure 7.** Spatial patterns of changes in Coefficient of Variation (CV) of (a) annual total ET, (b) annual total runoff (Q), (c) transpiration (TRANS), (d) bare soil evaporation (EVBS), (e) canopy water evaporation (EVCW), (f) snow sublimation (SBSNO) across the UCRB for GEOV2 product compared to default climatologic GVF parameterization.

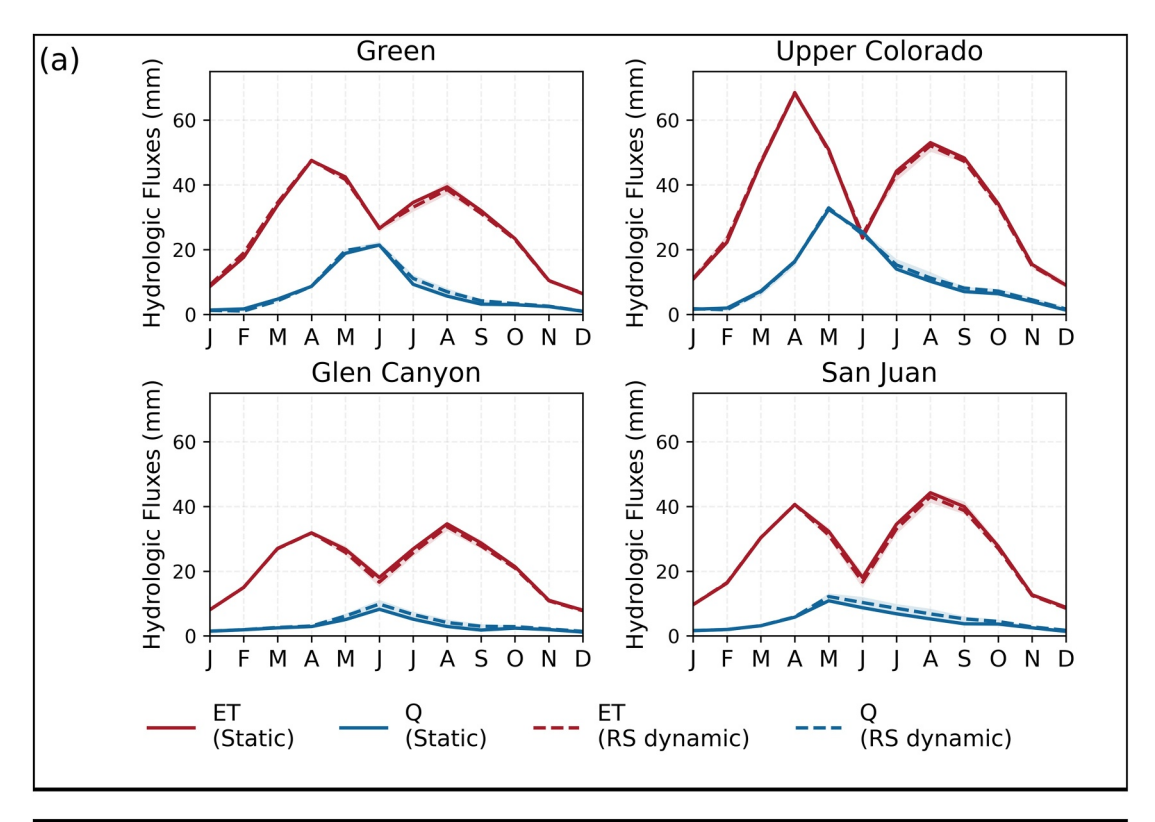
#### 3.2.2. Impacts of GVF Interannual Variability on Hydrologic Seasonality

Differences in the seasonal patterns of hydrologic fluxes in four sub-basins of UCRB between the Noah LSM using monthly climatological GVF and dynamic parameterization are primarily in the growing season (April–September), as illustrated in Figure 8a and Figure S5 in Supporting Information S1. By incorporating satellite vegetation dynamics, the total ET and Q of Upper Colorado undergo changes, resulting in a reduction in total ET of approximately -3 to -1 mm among different GVF products between July and August and an increase in runoff by around 3 mm during late summer (Figure 8a). The total ET in the Green, another subbasin situated in the

LONGYANG AND ZENG 13 of 23

1944 7973, 2024, 9, Downloaded from https://agupubs.onlinelibrary.wiley.com/doi/10.1029/2023WR035662 by Arizona State University Acq. Wiley Online Library on [04/10/2024]. See the Terms and Conditions (https://onlinelibrary.wiley.com/dorns

and-conditions) on Wiley Online Library for rules of use; OA articles



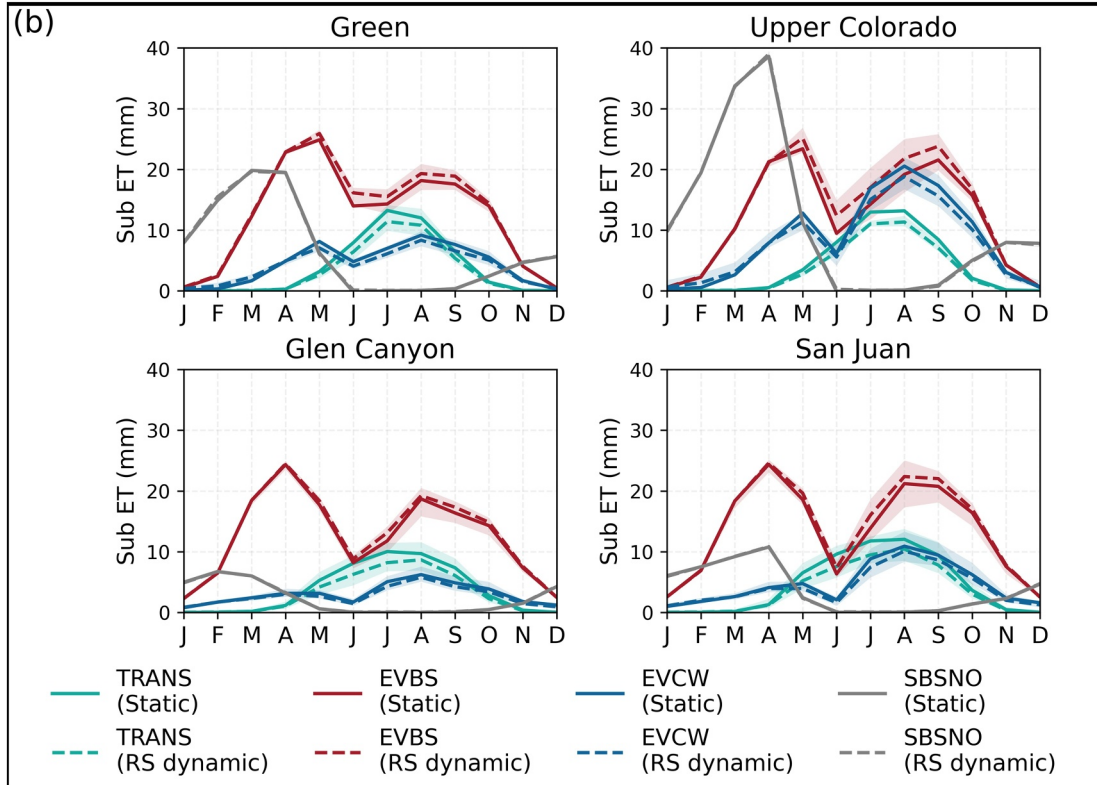


**Figure 8.** (a) Multi-year Domain Average Total ET and Total Runoff (Q) across the Four Subbasins Green, Upper Colorado, Glen Canyon and San Juan in the UCRB during 2001–2011. (b) Analogous to panel (a), but for subcomponents of ET, including transpiration (TRANS), bare soil evaporation (EVBS), canopy water evaporation (EVCW), and snow sublimation (SBSNO). Shading area depicts the uncertainties from the incorporation of seven remotely sensed GVF products, while the dashed line represents the median of these products.

LONGYANG AND ZENG 14 of 23

northern UCRB, is predominantly influenced by time-varying GVF changes from June and August. Integrating interannually dynamic GVF leads to a modest decrease in total ET for the two southern subbasins (i.e., Glen Canyon and San Juan), characterized by a bimodal pattern with peaks in April and August, while total runoff correspondingly increases.

An important seasonal feature of the UCRB is the bi-peak of bare soil evaporation and the single peak of transpiration, as shown in Figure 8b. The soil evaporation reaches the first peak in April or May with high soil moisture content due to snow melt, followed by the vegetation transpiration peaks in June or July. The bare soil evaporation has the second peak at the end of the growing season around August or September. Depending on the relative magnitude of bare soil evaporation and vegetation transpiration, the total ET has two peaks across all subbasins. In addition, bare soil evaporation is the largest among all ET components in the UCRB, and GVF directly changes the partitioning of total ET into bare soil evaporation and transpiration as indicated by Equation 2.

Interannually variant GVF does not markedly shift the seasonal phases of hydrologic variables but does induce moderate modifications in their magnitudes, particularly for the ET partitioning. The transpiration peak consistently occurs in July or August, with amounts ranging from 10 to 13 mm over years, and the differences resulting from the integration of remotely sensed GVF vary between -2 and +3 mm among different products (Figure S6 in Supporting Information S1). Compared to the northern subbasins (i.e., Green and Upper Colorado Figure 8a), vegetation transpiration experiences a more pronounced effect in the southern subbasins (i.e., Glen Canyon and San Juan in Figure 8b). Evaporation (both from bare soil and canopy surfaces) shows a larger alteration than transpiration in response to the year-to-year variable vegetation dynamics.

Uncertainties from remote sensing GVF products can propagate into total ET and runoff estimates, particularly evident in Upper Colorado during the late summer seasons (Figures 8a and Figure S5 in Supporting Information S1). These uncertainties become more prominent for ET subcomponent estimates, especially during growing seasons, as evident in Figures 8b and Figure S6 in Supporting Information S1, where the dashed lines, representing the median of the seven products, significantly diverge from the solid line (Noah LSM with static scheme). Such uncertainties, originating from various data sources, can be approximately interpreted as the sensitivity of hydrological flux variables to GVF changes. During non-growing seasons, these hydrologic variables display insensitivity to GVF changes. As shown in Figure 1 and Figure S4 in Supporting Information S1, during winter months, most of the remotely sensed GVF values used in this study are higher than the climatological GVF. However, the associated response of ET subcomponents is marginally affected by these differences (almost negligible), possibly due to that vegetation growth activity, which plays a role in energy partitioning processes, is inactive during wintertime. In summary, from April to August, dynamic vegetation changes influence total ET by reallocating among ET subcomponents (mainly affecting bare soil evaporation), consequently impacting runoff in the UCRB and its four subbasins.

#### 4. Discussion

#### 4.1. Interactions Between Parameters for LSMs After Updating Vegetation Information

While satellite products may more accurately reflect actual vegetation conditions, incorporating remotely sensed vegetation dynamics into the process-based Noah LSM does not automatically enhance the realism of the model. In this study, combined with the calibrated soil parameters, the performance of simulated streamflow even degrades after substituting the climatological GVF with an interannually varying GVF (Figure S10 in Supporting Information S1). This can be attributed that data integration can modify the parameter-hydrologic component relationships within the model. These changes can manifest in two different ways. On one hand, vegetation in LSMs is a key determinant of the physical process how energy and water are distributed between biotic and abiotic components, thereby directly influencing hydrologic flux estimates (e.g., as Equations 2–4 shows in this study). On the other hand, parameters can interact with each other within the model. For example, the presence of vegetation can influence soil physicochemical characteristics, such as hydraulic conductivity and soil porosity (Qiu et al., 2022; Y. W. Zhang et al., 2021). Concurrently, vegetation tends to adapt to different soil types (George et al., 2012; Rao et al., 2016), indicating that the physical and chemical properties of the soil can also significantly shape and affect the type of vegetation that thrives. When vegetation information is changed from a climatologic to a dynamic parameterization, the interactions between vegetation and soil parameters correspondingly alter, therefore leading to alterations in hydrologic estimates. Hence, the updating vegetation-related parameterization

LONGYANG AND ZENG 15 of 23

using time-varying satellite products may require model parameter recalibration (e.g., saturated hydraulic conductivity, saturated soil potential, minimum stomatal resistance, and roughness length) and a re-evaluation of certain model assumptions (e.g., snow shading by high vegetation) (Nogueira et al., 2021; Ruiz-Vásquez et al., 2023).

Another concern arises from the uncertainty inherent in remotely sensed vegetation products. As discussed in Section 3.2, spatial variations in vegetation indices can be propagated to the subsequent estimates in hydrologic components and their interannual variability, leading to significant discrepancies among diverse satellite products. This presents a challenge in confidently updating LSM parameterization with dynamic vegetation data from a specific satellite product, as it is hard to guarantee the accuracy and reality of the selected one. For example, in this study, we calibrate the soil parameter based on the climatologic GVF that may be considered "biased" compared to any yearly varied remotely sensed GVF. It may also introduce bias into the calibrated soil parameter, thereby resulting in degraded performance in streamflow simulation. A feasible approach may be to employ multi-objective optimization in LSM calibration (Denager et al., 2023; Mostafaie et al., 2018). By extending the calibration targets beyond streamflow to include variables like Land Surface Temperature (LST) or SWE, the calibration process could become more comprehensive.

In this study, the direct updating of vegetation information is considered a highly simplified form of data assimilation. Data assimilation enhances model accuracy by dynamically integrating real-time observational data from various sources, continuously adjusting model states to closely align with observed realities (X. Li et al., 2024). In contrast, our approach (referred to as "direct insertion"), is less complex and occurs less frequently, thereby reducing computational demands compared to standard data assimilation processes that require constant data input and processing. Nevertheless, this simplified method may not be as effective at capturing the nuanced dynamics within model states. Although it is a very simple method and not a substitute for full-scale data assimilation, direct insertion does not require any unbiasedness assumptions to operate optimally, unlike more sophisticated techniques such as Kalman Filters. Given that biases in atmospheric forcing (particularly precipitation) are often large and unknown (blind bias) in data-scarce regions, direct insertion represents a unique approach to improving the estimation of land surface variables by assimilating vegetation observations (Rahman et al., 2020).

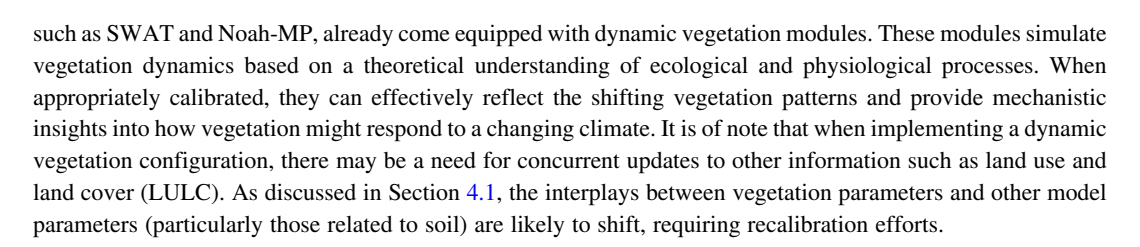
#### 4.2. Implication for Climate Change Assessment

As UCRB generates around 90% of runoff for the CRB, understanding the responses of vegetation to climate change and forest management is fundamental to the water security of the southwestern US. This study demonstrates the importance of dynamic GVF parameterization which alters the redistribution of precipitation among hydrologic fluxes, their interannual variabilities and seasonal patterns throughout the UCRB. Though remotely sensed products do not show vegetation long-term trends during the last decades in UCRB, future climate conditions may introduce gradual or abrupt changes in vegetation parameterization.

Climate changes can introduce adaptive responses in vegetation that provide feedback to the climate system (Ramstein et al., 2017). It implies that future vegetation phenology and type distribution may substantially differ from the historical patterns, for example, earlier greening (Lian et al., 2020), longer duration of the active vegetation-growing season (Grossiord et al., 2022; Kunkel et al., 2004; Q. Liu et al., 2018), shifts in vegetation types (Kelly & Goulden, 2008; Sturm et al., 2001). Although some earth system models that provide climate change projections already incorporate dynamic models of vegetation or land cover (e.g., MIROC-ESM, HadGEM2-ES, IPSL-CM5B-LR), in offline LSMs or large hydrological models, the common practice has been to use LAI/GVF climatology derived from multi-year monthly averages over historical periods (Christensen & Lettenmaier, 2007; Christensen et al., 2004; Currier et al., 2023; Harding et al., 2012). Static configurations may not adequately capture the potential dynamic changes in vegetation over a long-term future projection, thereby challenging its predictability under climate change. Inadequate representations of vegetation dynamics in hydrological models and uncoupled LSMs potentially result in biased estimations of water availability.

It is worthwhile to consider replacing static vegetation climatology with time-varying vegetation characteristics in model configurations for more reliable climate change assessments. A feasible way involves establishing a statistically based empirical relationship using satellite-derived vegetation indices. Grounded in observational data, it allows the models to capture the evolving vegetation dynamics projected into the far future, although the extrapolation of past observations to the future does come with inherent uncertainty. Alternatively, some models,

LONGYANG AND ZENG 16 of 23



#### 4.3. Deep Learning-Based Surrogate Model for LSMs

In physically based LSM model computing, the runoff generation process in grid cells generally operates independently without lateral interaction and is therefore feasibly parallelizable. Likewise, deep learning calculations can be efficiently executed on GPUs in batches, significantly reducing computational time costs. In this study, a single forward run for all UCRB grid cells (over 2,000 at a 1/8th degree spatial resolution) during the entire simulation period (1979–2016) on a daily scale with the LSTM emulator takes mere ~4 s using a single NVIDIA Quadro RTX 5000 GPU. This approach accelerates the parameter calibration process in our study, highlighting the effectiveness of deep learning-based surrogate models in expediting uncertainty quantification for process-based, distributed hydrological models, which typically demand substantial computational resources.

For successful surrogate model applications, both speed and accuracy are essential, necessitating large amounts of training data to achieve the required accuracy in replicating simulation outputs when constructing machine learning emulators (Kasim et al., 2021). The computational cost challenges shift toward building a high-fidelity emulator with a limited range of training data. On one hand, the effectiveness of surrogate models in capturing the relationship between hydrologic inputs and outputs hinges on selecting an appropriate sampling approach and a suitable sample size. While we utilized LHS to generate 1,000 parameter samples in our study, a smaller sample size, approximately 20 times the number of parameters, is often adequate for pinpointing sensitive parameters (H. Wang et al., 2023). This can further facilitate the more streamlined construction of the surrogate within a given uncertainty quantification framework, especially when constructing surrogate models at regional to continental scales with high spatial heterogeneity. On the other hand, the machine learning model architecture is crucial. The right architecture provides suitable priors for a given problem. As discussed in Section 2.3, LSTM-type architectures are well-suited for emulating surface hydrologic process model physics due to their similar structures involving outputs and states, whereas convolutional architectures (CNN) are natural solvers for Partial Differential Equations (PDE) and suitable for groundwater modeling surrogates. Combining the strengths of LSTM and CNN presents a novel possibility for building distributed hydrological model emulators (e.g., M. Tang et al., 2021; S. Yang, Yang, & Chen, 2019; Y. Yang, Pan, et al., 2019), which could capture the spatiotemporal dynamics between hydrologic responses and predictors, particularly in cases involving surface-groundwater interactions.

Surrogate models exhibiting high accuracy can adeptly mimic the physics of specific process-based models, thereby expediting parameter calibration. This advantage can also be harnessed to the model recalibration process after replacing the static climatological parameterization with the time-varying satellite data set. Nevertheless, surrogate-based parameter calibration has limitations. Firstly, there is a possibility of bias in surrogate models, as they may not fully replicate the complex processes of the original models. If the surrogate does not exactly represent the interplay between parameters and hydrologic inputs, the calibrated parameter derived from a biased surrogate could also be biased. Secondly, surrogates cannot address the intrinsic limitations of process-based models. For example, surrogate-based calibration does not inherently resolve the equifinality (i.e., different parameter combinations produce similar results, Beven, 2006) dilemma. As noted in Section 4.1, even with further recalibration efforts, the use of different remotely sensed vegetation products in place of climatological parameterization could lead to vastly different recalibrated parameter sets, though they may yield very similar evaluation metrics. Additionally, site-specific calibration often results in inconsistent and non-contiguous parameters across geographically similar, adjacent areas (S. Yang, Yang, & Chen, 2019; Y. Yang, Pan, et al., 2019). This issue also remains unresolved with surrogate-based calibration. In response, recent developments like the differentiable parameter learning (dPL) approach proposed by Tsai et al. (2021) offer a novel method. This method bypasses traditional calibration, instead utilizing deep learning platforms to expedite parameter estimation (the hydrologic models have been directly implemented in the platforms supporting automatic

LONGYANG AND ZENG 17 of 23

differentiation). It preserves the physical integrity of the hydrologic processes and derives more meaningful and coherent parameter sets based on regional information.

Although surrogate-based parameter calibration has its drawbacks, it still serves as an efficient tool for complex or computationally expensive models, such as Variable Infiltration Capacity (VIC, Liang et al., 1994) or other distributed models (Tsai et al., 2021). It is particularly relevant considering the effort required to translate original LSMs (typically written in Fortran, C, or C++) into Python for implementation in deep learning platforms.

Besides parameter calibration, the highly accurate surrogate model can be effectively employed as a diagnostic tool for generating hydrologic predictions. This enables easy implementation of data fusion and assimilation. Such a model simplifies the process of substituting specific data chunks, which may be challenging to integrate into a process-based model without extensive code modifications. This flexibility can broaden the scope for exploring new scientific questions. A practical example is the web-based HydroGEN platform (Condon et al., 2021). The platform employs ML emulators to generate user-tailored seasonal to annual hydrologic scenarios for both groundwater and surface water systems by leveraging observations and advanced physics-based hydrologic models.

#### 5. Conclusions

In this study, we quantify the impacts of dynamically varying vegetation on the spatial and temporal patterns of hydrologic processes, using the UCRB as a test case. The machine learning-based surrogate model accurately reproduces the physical processes represented by Noah LSM and allows computationally efficient fusing of vegetation parameters (i.e., GVF in this study) from multiple remotely sensed products. Without considering year-to-year variable vegetation dynamics, the static monthly climatological GVF configuration of Noah LSM misses the vegetation response to hydroclimatic variability, leading to underestimated water yield (as much as 14%). In this semi-arid and arid UCRB, various remote sensing products consistently predict that changes in biotic ET components (i.e., transpiration and canopy evaporation) outweigh the changes in abiotic ET components (i.e., bare soil evaporation). As the abiotic ET component exhibits two peaks in April and August and biotic ET components have a single peak in July, the static monthly climatological GVF in Noah LSM may not fully represent the seasonal patterns in the UCRB.

Through incorporating satellite-derived time-varying vegetation indices into Noah LSM, this study highlights the importance of representing the response of vegetation to climate forcing variability. This study also highlights the additional two mechanisms of vegetation in modifying hydrologic fluxes by (a) buffering effect to the climate interannual variability and (b) modifying the hydrologic seasonal patterns with different biotic and abiotic ET components. Therefore, vegetation responses to climate should be explicitly (either statistically or mechanistically) represented to predict the future hydrologic changes in the UCRB.

#### **Appendix A: List of Formulas**

Appendix A1 provides the details of the Long-Short Term Memory (LSTM) cell calculations, and Appendix A2 presents the performance evaluation metrics used in this study.

#### A1. Long-Short Term Memory (LSTM) Cell

The Long-Short Term Memory (LSTM) computations are expressed as

$$i_t = \sigma(W_{xi} \cdot x_t + W_{hi} \cdot h_{t-1} + b_i)$$

$$f_t = \sigma(W_{xf} \cdot x_t + W_{hf} \cdot h_{t-1} + b_f)$$

$$g_t = \tanh(W_{xg} \cdot x_t + W_{hg} \cdot h_{t-1} + b_g)$$

$$o_t = \sigma(W_{xo} \cdot x_t + W_{ho} \cdot h_{t-1} + b_o)$$

$$c_t = f_t \odot c_{t-1} + i_t \odot g_t$$

$$h_t = o_t \odot \tanh(c_t)$$

LONGYANG AND ZENG 18 of 23

.com/doi/10.1029/2023WR035662 by Arizona State University Acq, Wiley Online

where  $W_{xi}$ ,  $W_{xf}$ ,  $W_{xg}$ , and  $W_{xo}$  are learnable weights of inputs  $x_i$ ,  $W_{hi}$ ,  $W_{hf}$ ,  $W_{hg}$ , and  $W_{ho}$  are learnable weights of the previous hidden states  $h_t$ , and  $b_i$ ,  $b_f$ ,  $b_o$ , and  $b_g$  are biases of the four gates, respectively.  $\sigma$  means sigmoid function, tanh is hyperbolic tangent function, and ① represents element-wise multiplication.

#### **A2. Performance Evaluation Metrics**

NSE = 1 - 
$$\frac{\sum_{t=1}^{T} (y_t - \hat{y}_t)^2}{\sum_{t=1}^{T} (y_t - \overline{y}_t)^2}$$

$$RMSE = \sqrt{\frac{\sum_{t=1}^{T} (y_t - \hat{y}_t)^2}{T}}$$

$$PBIAS = \frac{1}{T} \sum_{t=1}^{T} \frac{y_t - \hat{y}_t}{y_t} \times 100$$

where  $y_t$  is a subcomponent ET or runoff estimation of Noah LSM at the time step t,  $\hat{y}_t$  is the subcomponent ET or runoff simulated by LSTM surrogate model at the time step t.

## **Data Availability Statement**

All data used in this research and the LSTM code are publicly available at https://www.hydroshare.org/resource/ f32010b5edc34e519399e2417db2cce6/. The United States Bureau of Reclamation (USBR) naturalized flow records can be found at https://www.usbr.gov/lc/region/g4000/NaturalFlow/provisional.html.

#### References

Amenu, G. G., & Kumar, P. (2008). A model for hydraulic redistribution incorporating coupled soil-root moisture transport, Hydrology and Earth System Sciences, 12(1), 55-74. https://doi.org/10.5194/hess-12-55-2008

Anderson, J. T., & Song, B. H. (2020). Plant adaptation to climate change—Where are we? Journal of Systematics and Evolution, 58(5), 533-545. https://doi.org/10.1111/ise.12649

Asher, M. J., Croke, B. F., Jakeman, A. J., & Peeters, L. J. (2015). A review of surrogate models and their application to groundwater modeling. Water Resources Research, 51(8), 5957-5973. https://doi.org/10.1002/2015wr016967

Babaeian, E., Paheding, S., Siddique, N., Devabhaktuni, V. K., & Tuller, M. (2022). Short-and mid-term forecasts of actual evapotranspiration with deep learning. Journal of Hydrology, 612, 128078. https://doi.org/10.1016/j.jhydrol.2022.128078

Barron-Gafford, G. A., Sanchez-Cañete, E. P., Minor, R. L., Hendryx, S. M., Lee, E., Sutter, L. F., et al. (2017). Impacts of hydraulic redistribution on grass-tree competition vs facilitation in a semi-arid savanna. New Phytologist, 215(4), 1451-1461. https://doi.org/10.1111/nph.14693

Beven, K. (2006). A manifesto for the equifinality thesis. Journal of Hydrology, 320(1-2), 18-36. https://doi.org/10.1016/j.jhydrol.2005.07.007 Bonan, G. B. (2008). Forests and climate change: Forcings, feedbacks, and the climate benefits of forests. Science, 320(5882), 1444-1449. https:// doi.org/10.1126/science.1155121

Boulton, C. A., Lenton, T. M., & Boers, N. (2022). Pronounced loss of Amazon rainforest resilience since the early 2000s. Nature Climate Change, 12(3), 271-278. https://doi.org/10.1038/s41558-022-01287-8

Chen, C., Park, T., Wang, X., Piao, S., Xu, B., Chaturvedi, R. K., et al. (2019). China and India lead in greening of the world through land-use management. Nature Sustainability, 2(2), 122-129. https://doi.org/10.1038/s41893-019-0220-7

Chen, F., & Dudhia, J. (2001). Coupling an advanced land surface-hydrology model with the Penn State-NCAR MM5 modeling system. Part I: Model implementation and sensitivity. Monthly Weather Review, 129(4), 569-585. https://doi.org/10.1175/1520-0493(2001)129<0569:

Chen, F., Mitchell, K., Schaake, J., Xue, Y., Pan, H. L., Koren, V., et al. (1996). Modeling of land surface evaporation by four schemes and comparison with FIFE observations. Journal of Geophysical Research, 101(D3), 7251-7268. https://doi.org/10.1029/95jd02165

Chen, J. M., Ju, W., Ciais, P., Viovy, N., Liu, R., Liu, Y., & Lu, X. (2019). Vegetation structural change since 1981 significantly enhanced the terrestrial carbon sink. Nature Communications, 10(1), 4259. https://doi.org/10.1038/s41467-019-12257-8

Christensen, N. S., & Lettenmaier, D. P. (2007). A multimodel ensemble approach to assessment of climate change impacts on the hydrology and water resources of the Colorado River Basin. Hydrology and Earth System Sciences, 11(4), 1417-1434. https://doi.org/10.5194/hess-11-1417-

Christensen, N. S., Wood, A. W., Voisin, N., Lettenmaier, D. P., & Palmer, R. N. (2004). The effects of climate change on the hydrology and water resources of the Colorado River basin. Climatic Change, 62(1-3), 337-363. https://doi.org/10.1023/b:clim.0000013684.13621.1f

# Acknowledgments

The research is supported by NSF CBET Award No. 2239621 and NSF GC Award No. 2330525. We greatly appreciate the reviewers' comments that help to improve this study.

LONGYANG AND ZENG 19 of 23

- Cihlar, J., Chen, J., & Li, Z. (1997). On the validation of satellite-derived products for land applications. *Canadian Journal of Remote Sensing*, 23(4), 381–389. https://doi.org/10.1080/07038992.1997.10855223
- Claverie, M., Matthews, J. L., Vermote, E. F., & Justice, C. O. (2016). A 30+ year AVHRR LAI and FAPAR climate data record: Algorithm description and validation. *Remote Sensing*, 8(3), 263. https://doi.org/10.3390/rs8030263
- Coenders-Gerrits, A. M. J., Van der Ent, R. J., Bogaard, T. A., Wang-Erlandsson, L., Hrachowitz, M., & Savenije, H. H. G. (2014). Uncertainties in transpiration estimates. *Nature*, 506(7487), E1–E2. https://doi.org/10.1038/nature12925
- Cohen, M., Christian-Smith, J., & Berggren, J. (2013). Water to supply the land: Irrigated agriculture in the Colorado River Basin, Oakland, CA. Pacific Institute.
- Condon, L., Maxwell, R., Bansal, V., Bearup, L., Chennault, C., Gallagher, L., et al. (2021). Lessons learned designing the HydroGEN machine learning platform for hydrologic exploration: A story of collaboration between hydrologic scientists, software developers, machine learning researchers and water managers. In AGU Fall Meeting Abstracts (Vol. 2021, p. SY24A-04).
- Currier, W. R., Wood, A. W., Mizukami, N., Nijssen, B., Hamman, J. J., & Gutmann, E. D. (2023). Vegetation representation influences projected streamflow changes in the Colorado River Basin. *Journal of Hydrometeorology*, 24(7), 1291–1310. https://doi.org/10.1175/jhm-d-22-0143.1
- Dannenberg, M. P., Wise, E. K., & Smith, W. K. (2019). Reduced tree growth in the semiarid United States due to asymmetric responses to intensifying precipitation extremes. *Science Advances*, 5(10), eaaw0667. https://doi.org/10.1126/sciadv.aaw0667
- Denager, T., Sonnenborg, T. O., Looms, M. C., Bogena, H., & Jensen, K. H. (2023). Point-scale multi-objective calibration of the Community Land Model (version 5.0) using in situ observations of water and energy fluxes and variables. *Hydrology and Earth System Sciences*, 27(14), 2827–2845. https://doi.org/10.5194/hess-27-2827-2023
- Ding, H., & Zhu, Y. (2018). NDE vegetation products system algorithm theoretical basis document, version 4.0. NOAA/NESDIS/OSPO. Retrieved from https://www.ospo.noaa.gov/Products/documents/GVF\_ATBD\_V4.0.pdf
- Duarte, C. M., Losada, I. J., Hendriks, I. E., Mazarrasa, I., & Marbà, N. (2013). The role of coastal plant communities for climate change mitigation and adaptation. *Nature Climate Change*, 3(11), 961–968. https://doi.org/10.1038/nclimate1970
- Duveiller, G., Hooker, J., & Cescatti, A. (2018). The mark of vegetation change on Earth's surface energy balance. *Nature Communications*, 9(1), 1–12. https://doi.org/10.1038/s41467-017-02810-8
- Ek, M. B., Mitchell, K. E., Lin, Y., Rogers, E., Grunmann, P., Koren, V., et al. (2003). Implementation of Noah land surface model advances in the National Centers for Environmental Prediction operational mesoscale Eta model. *Journal of Geophysical Research*, 108(D22), 8851. https://doi.org/10.1029/2002jd003296
- Elmer, N. J., Mecikalski, J. R., Molthan, A. L., Gochis, D. J., & Nair, U. (2022). Impact of real-time satellite-derived green vegetation fraction on national water model fluxes in humid Alabama Watersheds. *JAWRA Journal of the American Water Resources Association*, 58(1), 104–118. https://doi.org/10.1111/1752-1688.12982
- Feng, D., Fang, K., & Shen, C. (2020). Enhancing streamflow forecast and extracting insights using long-short term memory networks with data integration at continental scales. Water Resources Research, 56(9), e2019WR026793. https://doi.org/10.1029/2019wr026793
- Ficklin, D. L., Stewart, I. T., & Maurer, E. P. (2013). Climate change impacts on streamflow and subbasin-scale hydrology in the Upper Colorado River Basin. *PLoS One*, 8(8), e71297. https://doi.org/10.1371/journal.pone.0071297
- George, E., Horst, W. J., & Neumann, E. (2012). Adaptation of plants to adverse chemical soil conditions. In Marschner's mineral nutrition of higher plants (pp. 409–472). Academic press.
- Good, S. P., Noone, D., & Bowen, G. (2015). Hydrologic connectivity constrains partitioning of global terrestrial water fluxes. Science, 349(6244), 175–177. https://doi.org/10.1126/science.aaa5931
- Grossiord, C., Bachofen, C., Gisler, J., Mas, E., Vitasse, Y., & Didion-Gency, M. (2022). Warming may extend tree growing seasons and compensate for reduced carbon uptake during dry periods. *Journal of Ecology*, 110(7), 1575–1589. https://doi.org/10.1111/1365-2745.13892
   Gutman, G., & Ignatov, A. (1998). The derivation of the green vegetation fraction from NOAA/AVHRR data for use in numerical weather
- prediction models. *International Journal of Remote Sensing*, 19(8), 1533–1543. https://doi.org/10.1080/014311698215333

  Harding, B. L., Wood, A. W., & Prairie, J. R. (2012). The implications of climate change scenario selection for future streamflow projection in the
- Upper Colorado River Basin. Hydrology and Earth System Sciences, 16(11), 3989–4007. https://doi.org/10.5194/hess-16-3989-2012 Hibbert, A. R. (1979). In Managing vegetation to increase flow in the Colorado River Basin (Vol. 66). Rocky Mountain Forest and Range
- Experiment Station, Forest Service, US Department of Agriculture. Hochreiter, S., & Schmidhuber, J. (1997). Long short-term memory. *Neural Computation*, 9(8), 1735–1780. https://doi.org/10.1162/neco.1997.9.
- Jacobs, J. (2011). The sustainability of water resources in the Colorado River basin. Bridge, 41(4), 6-12.
- Jia, W., Zhang, Y., Wei, Z., Zheng, Z., & Xie, P. (2023). Daily reference evapotranspiration prediction for irrigation scheduling decisions based on the hybrid PSO-LSTM model. PLoS One, 18(4), e0281478. https://doi.org/10.1371/journal.pone.0281478
- Jiang, Z., Vargas, M., & Csiszar, I. (2016). New operational real-time daily rolling weekly Green Vegetation fraction product derived from suomi NPP VIIRS reflectance data. In 2016 IEEE International Geoscience and Remote Sensing Symposium (IGARSS) (pp. 3524–3527). IEEE.
- Kasim, M. F., Watson-Parris, D., Deaconu, L., Oliver, S., Hatfield, P., Froula, D. H., et al. (2021). Building high accuracy emulators for scientific simulations with deep neural architecture search. *Machine Learning: Science and Technology*, 3(1), 015013. https://doi.org/10.1088/2632-2153/ac3ffa
- Kelly, A. E., & Goulden, M. L. (2008). Rapid shifts in plant distribution with recent climate change. Proceedings of the National Academy of Sciences of the United States of America, 105(33), 11823–11826. https://doi.org/10.1073/pnas.0802891105
- Kingma, D. P., & Ba, J. (2014). Adam: A method for stochastic optimization. arXiv preprint arXiv:1412.6980.
- Kolassa, J., Reichle, R. H., Koster, R. D., Liu, Q., Mahanama, S., & Zeng, F. W. (2020). An observation-driven approach to improve vegetation phenology in a global land surface model. *Journal of Advances in Modeling Earth Systems*, 12(9), e2020MS002083. https://doi.org/10.1029/ 2020ms002083
- Konings, A. G., & Gentine, P. (2017). Global variations in ecosystem-scale isohydricity. Global Change Biology, 23(2), 891–905. https://doi.org/10.1111/gcb.13389
- Koster, R. D., Walker, G. K., Collatz, G. J., & Thornton, P. E. (2014). Hydroclimatic controls on the means and variability of vegetation phenology and carbon uptake. *Journal of Climate*, 27(14), 5632–5652. https://doi.org/10.1175/jcli-d-13-00477.1
- Kratzert, F., Klotz, D., Brenner, C., Schulz, K., & Herrnegger, M. (2018). Rainfall–runoff modelling using Long Short-Term Memory (LSTM) networks. *Hydrology and Earth System Sciences*, 22(11), 6005–6022. https://doi.org/10.5194/hess-22-6005-2018
- Kratzert, F., Klotz, D., Shalev, G., Klambauer, G., Hochreiter, S., & Nearing, G. (2019). Towards learning universal, regional, and local hydrological behaviors via machine learning applied to large-sample datasets. *Hydrology and Earth System Sciences*, 23(12), 5089–5110. https://doi.org/10.5194/hess-23-5089-2019

LONGYANG AND ZENG 20 of 23



- Kumar, S. V., Mocko, D. M., Wang, S., Peters-Lidard, C. D., & Borak, J. (2019). Assimilation of remotely sensed leaf area index into the Noah-MP land surface model: Impacts on water and carbon fluxes and states over the continental United States. *Journal of Hydrometeorology*, 20(7), 1359–1377. https://doi.org/10.1175/jhm-d-18-0237.1
- Kumar, S. V., Peters-Lidard, C. D., Tian, Y., Houser, P. R., Geiger, J., Olden, S., et al. (2006). Land information system: An interoperable framework for high resolution land surface modeling. *Environmental Modelling & Software*, 21(10), 1402–1415. https://doi.org/10.1016/j.envsoft 2005.07.004
- Kumar, S. V., Wang, S., Mocko, D. M., Peters-Lidard, C. D., & Xia, Y. (2017). Similarity assessment of land surface model outputs in the North American land data assimilation system. Water Resources Research, 53(11), 8941–8965. https://doi.org/10.1002/2017wr020635
- Kunkel, K. E., Easterling, D. R., Hubbard, K., & Redmond, K. (2004). Temporal variations in frost-free season in the United States: 1895–2000. Geophysical Research Letters, 31(3), L03201. https://doi.org/10.1029/2003gl018624
- Lee, E., Zeng, F. W., Koster, R. D., Weir, B., Ott, L. E., & Poulter, B. (2018). The impact of spatiotemporal variability in atmospheric CO<sub>2</sub> concentration on global terrestrial carbon fluxes. *Biogeosciences*, 15(18), 5635–5652. https://doi.org/10.5194/bg-15-5635-2018
- Li, D., Wrzesien, M. L., Durand, M., Adam, J., & Lettenmaier, D. P. (2017). How much runoff originates as snow in the western United States, and how will that change in the future? *Geophysical Research Letters*, 44(12), 6163–6172. https://doi.org/10.1002/2017gl073551
- Li, Q., Zhu, Y., Shangguan, W., Wang, X., Li, L., & Yu, F. (2022). An attention-aware LSTM model for soil moisture and soil temperature prediction. *Geoderma*, 409, 115651. https://doi.org/10.1016/j.geoderma.2021.115651
- Li, X., Liu, F., Ma, C., Hou, J., Zheng, D., Ma, H., et al. (2024). Land data assimilation: Harmonizing theory and data in land surface process studies. *Reviews of Geophysics*, 62(1), e2022RG000801. https://doi.org/10.1029/2022re000801
- Lian, X., Piao, S., Li, L. Z., Li, Y., Huntingford, C., Ciais, P., et al. (2020). Summer soil drying exacerbated by earlier spring greening of northern vegetation. *Science Advances*, 6(1), eaax0255. https://doi.org/10.1126/sciadv.aax0255
- Liang, X., Lettenmaier, D. P., Wood, E. F., & Burges, S. J. (1994). A simple hydrologically based model of land surface water and energy fluxes
- for general circulation models. *Journal of Geophysical Research*, 99(D7), 14415–14428. https://doi.org/10.1029/94jd00483 Link, T. E., & Marks, D. (1999). Point simulation of seasonal snow cover dynamics beneath boreal forest canopies. *Journal of Geophysical*
- Research, 104(D22), 27841–27857.
  Liu, Q., Piao, S., Janssens, I. A., Fu, Y., Peng, S., Lian, X. U., et al. (2018). Extension of the growing season increases vegetation exposure to frost.
- Nature Communications, 9(1), 426. https://doi.org/10.1038/s41467-017-02690-y
  Liu, Y., Liu, R., & Chen, J. M. (2012). Retrospective retrieval of long-term consistent global leaf area index (1981–2011) from combined AVHRR
- and MODIS data. Journal of Geophysical Research, 117(G4), G04003. https://doi.org/10.1029/2012jg002084
- Livneh, B., Xia, Y., Mitchell, K. E., Ek, M. B., & Lettenmaier, D. P. (2010). Noah LSM snow model diagnostics and enhancements. *Journal of Hydrometeorology*, 11(3), 721–738. https://doi.org/10.1175/2009jhm1174.1
- Ma, K., Feng, D., Lawson, K., Tsai, W. P., Liang, C., Huang, X., et al. (2021). Transferring hydrologic data across continents—leveraging data-rich regions to improve hydrologic prediction in data-sparse regions. Water Resources Research, 57(5), e2020WR028600. https://doi.org/10.1029/2020wr028600
- Ma, T., Duan, Z., Li, R., & Song, X. (2019). Enhancing SWAT with remotely sensed LAI for improved modelling of ecohydrological process in subtropics. *Journal of Hydrology*, 570, 802–815. https://doi.org/10.1016/j.jhydrol.2019.01.024
- Mahrt, L., & Ek, M. (1984). The influence of atmospheric stability on potential evaporation. *Journal of Applied Meteorology and Climatology*, 23(2), 222–234. https://doi.org/10.1175/1520-0450(1984)023<0222:tioaso>2.0.co;2
- Malle, J., Rutter, N., Mazzotti, G., & Jonas, T. (2019). Shading by trees and fractional snow cover control the subcanopy radiation budget. *Journal of Geophysical Research: Atmospheres*, 124(6), 3195–3207. https://doi.org/10.1029/2018jd029908
- Maxwell, R. M., Condon, L. E., & Melchior, P. (2021). A physics-informed, machine learning emulator of a 2d surface water model: What temporal networks and simulation-based inference can help us learn about hydrologic processes. *Water*, 13(24), 3633. https://doi.org/10.3390/w13243633
- McCabe, G. J., & Wolock, D. M. (2020). The water-year water balance of the Colorado River Basin. JAWRA Journal of the American Water Resources Association, 56(4), 724–737. https://doi.org/10.1111/1752-1688.12848
- Meyal, A. Y., Versteeg, R., Alper, E., Johnson, D., Rodzianko, A., Franklin, M., & Wainwright, H. (2020). Automated cloud based long short-term memory neural network based SWE prediction. Frontiers in Water, 2, 574917. https://doi.org/10.3389/frwa.2020.574917
- Miller, J., Barlage, M., Zeng, X., Wei, H., Mitchell, K., & Tarpley, D. (2006). Sensitivity of the NCEP/Noah land surface model to the MODIS green vegetation fraction data set. *Geophysical Research Letters*, 33(13), L13404. https://doi.org/10.1029/2006gl026636
- Miranda, J. D. D., Armas, C., Padilla, F. M., & Pugnaire, F. I. (2011). Climatic change and rainfall patterns: Effects on semi-arid plant communities of the Iberian Southeast. *Journal of Arid Environments*, 75(12), 1302–1309. https://doi.org/10.1016/j.jaridenv.2011.04.022
- Mostafaie, A., Forootan, E., Safari, A., & Schumacher, M. (2018). Comparing multi-objective optimization techniques to calibrate a conceptual hydrological model using in situ runoff and daily GRACE data. Computational Geosciences, 22(3), 789–814. https://doi.org/10.1007/s10596-018-9726-8
- Murray-Tortarolo, G., Anav, A., Friedlingstein, P., Sitch, S., Piao, S., Zhu, Z., et al. (2013). Evaluation of land surface models in reproducing satellite-derived LAI over the high-latitude Northern Hemisphere. Part I: Uncoupled DGVMs. Remote Sensing, 5(10), 4819–4838. https://doi.org/10.3390/rs5104819
- Nash, J. E., & Sutcliffe, J. V. (1970). River flow forecasting through conceptual models: Part I—A discussion of principles. *Journal of Hydrology*, 10(3), 282–290. https://doi.org/10.1016/0022-1694(70)90255-6
- Niu, G. Y., Yang, Z. L., Mitchell, K. E., Chen, F., Ek, M. B., Barlage, M., et al. (2011). The community Noah land surface model with multi-parameterization options (Noah-MP): 1. Model description and evaluation with local-scale measurements. *Journal of Geophysical Research*, 116(D12), D12109. https://doi.org/10.1029/2010jd015139
- Nobre, C. A., Sampaio, G., Borma, L. S., Castilla-Rubio, J. C., Silva, J. S., & Cardoso, M. (2016). Land-use and climate change risks in the Amazon and the need of a novel sustainable development paradigm. *Proceedings of the National Academy of Sciences of the United States of America*, 113(39), 10759–10768. https://doi.org/10.1073/pnas.1605516113
- Nogueira, M., Boussetta, S., Balsamo, G., Albergel, C., Trigo, I. F., Johannsen, F., & Dutra, E. (2021). Upgrading land-cover and vegetation seasonality in the ECMWF coupled system: Verification with FLUXNET sites, METEOSAT satellite land surface temperatures, and ERA5 atmospheric reanalysis. *Journal of Geophysical Research: Atmospheres, 126*(15), e2020JD034163. https://doi.org/10.1029/2020jd034163
- Noilhan, J., & Planton, S. (1989). A simple parameterization of land surface processes for meteorological models. *Monthly Weather Review*, 117(3), 536–549. https://doi.org/10.1175/1520-0493(1989)117<0536:aspols>2.0.co;2
- Norman, J. M., Kustas, W. P., & Humes, K. S. (1995). Source approach for estimating soil and vegetation energy fluxes in observations of directional radiometric surface temperature. Agricultural and Forest Meteorology, 77(3-4), 263–293. https://doi.org/10.1016/0168-1923(95) 02265-y

LONGYANG AND ZENG 21 of 23

- Oehri, J., Schaepman-Strub, G., Kim, J. S., Grysko, R., Kropp, H., Grünberg, I., et al. (2022). Vegetation type is an important predictor of the arctic summer land surface energy budget. *Nature Communications*, 13(1), 6379. https://doi.org/10.1038/s41467-022-34049-3
- Orth, R. (2021). Global soil moisture data derived through machine learning trained with in-situ measurements. Scientific Data, 8(1), 1–14. https://doi.org/10.1038/s41597-021-00964-1
- Poulter, B., Frank, D., Ciais, P., Myneni, R. B., Andela, N., Bi, J., et al. (2014). Contribution of semi-arid ecosystems to interannual variability of the global carbon cycle. *Nature*, 509(7502), 600–603. https://doi.org/10.1038/nature13376
- Qiu, D., Xu, R., Wu, C., Mu, X., Zhao, G., & Gao, P. (2022). Vegetation restoration improves soil hydrological properties by regulating soil physicochemical properties in the Loess Plateau, China. *Journal of Hydrology*, 609, 127730. https://doi.org/10.1016/j.jhydrol.2022.127730
- Rahman, A., Zhang, X., Xue, Y., Houser, P., Sauer, T., Kumar, S., et al. (2020). A synthetic experiment to investigate the potential of assimilating LAI through direct insertion in a land surface model. *Journal of Hydrology*, *9*, 100063. https://doi.org/10.1016/j.hydroa.2020.100063
- Ramstein, G., de Boer, H., & Soh, W. K. (2017). Vegetation and climate interactions: An introduction. In EGU General Assembly Conference Abstracts (p. 19655).
- Rao, I. M., Miles, J. W., Beebe, S. E., & Horst, W. J. (2016). Root adaptations to soils with low fertility and aluminium toxicity. *Annals of Botany*, 118(4), 593–605. https://doi.org/10.1093/aob/mcw073
- Rodell, M., Houser, P. R., Berg, A. A., & Famiglietti, J. S. (2005). Evaluation of 10 methods for initializing a land surface model. *Journal of Hydrometeorology*, 6(2), 146–155. https://doi.org/10.1175/jhm414.1
- Ruhge, R. L., & Barlage, M. (2011). Integrating a real-time green vegetation fraction (GVF) product into the land information system (LIS). In 15th Symposium on Integrated Observing and Assimilation Systems for Atmosphere, Oceans, and Land Surface.
- Ruiz-Vásquez, M., O, S., Arduini, G., Boussetta, S., Brenning, A., Bastos, A., et al. (2023). Impact of updating vegetation information on land surface model performance. *Journal of Geophysical Research: Atmospheres*, 128(21), e2023JD039076. https://doi.org/10.1029/2023jd039076
- Schlesinger, W. H., & Jasechko, S. (2014). Transpiration in the global water cycle. Agricultural and Forest Meteorology, 189, 115–117. https://doi.org/10.1016/j.agrformet.2014.01.011
- Sha, Z., Bai, Y., Li, R., Lan, H., Zhang, X., Li, J., et al. (2022). The global carbon sink potential of terrestrial vegetation can be increased substantially by optimal land management. Communications Earth & Environment, 3(1), 8. https://doi.org/10.1038/s43247-021-00333-1
- Song, Y., Tsai, W. P., Gluck, J., Rhoades, A., Zarzycki, C., McCrary, R., et al. (2023). LSTM-based data integration to improve snow water equivalent prediction and diagnose error sources. *Journal of Hydrometeorology*, 25(1), 223–237. https://doi.org/10.1175/jhm-d-22-0220.1
- Sturm, M., Racine, C., & Tape, K. (2001). Increasing shrub abundance in the Arctic. *Nature*, 411(6837), 546–547. https://doi.org/10.1038/35079180
- Sun, L., Yang, L., Chen, L., Zhao, F., & Li, S. (2018). Hydraulic redistribution and its contribution to water retention during short-term drought in the summer rainy season in a humid area. *Journal of Hydrology*, 566, 377–385. https://doi.org/10.1016/j.jhydrol.2018.09.032
- Sun, R., Pan, B., & Duan, Q. (2023). A surrogate modeling method for distributed land surface hydrological models based on deep learning. Journal of Hydrology, 624, 129944. https://doi.org/10.1016/j.jhydrol.2023.129944
- Tang, M., Liu, Y., & Durlofsky, L. J. (2021). Deep-learning-based surrogate flow modeling and geological parameterization for data assimilation in 3D subsurface flow. Computer Methods in Applied Mechanics and Engineering, 376, 113636. https://doi.org/10.1016/j.cma.2020.113636
- Tang, Q., Vivoni, E. R., Muñoz-Arriola, F., & Lettenmaier, D. P. (2012). Predictability of evapotranspiration patterns using remotely sensed vegetation dynamics during the North American monsoon. *Journal of Hydrometeorology*, *13*(1), 103–121. https://doi.org/10.1175/jhm-d-11-032\_1
- Tesemma, Z. K., Wei, Y., Peel, M. C., & Western, A. W. (2015). The effect of year-to-year variability of leaf area index on Variable Infiltration Capacity model performance and simulation of runoff. *Advances in Water Resources*, 83, 310–322. https://doi.org/10.1016/j.advwatres.2015.
- Thorne, J. H., Choe, H., Boynton, R. M., Bjorkman, J., Albright, W., Nydick, K., et al. (2017). The impact of climate change uncertainty on California's vegetation and adaptation management. *Ecosphere*, 8(12), e02021. https://doi.org/10.1002/ecs2.2021
- Tran, H., Leonarduzzi, E., De la Fuente, L., Hull, R. B., Bansal, V., Chennault, C., et al. (2021). Development of a deep learning emulator for a distributed groundwater–surface water model: ParFLOW-ML. Water, 13(23), 3393. https://doi.org/10.3390/w13233393
- Tran, H., Zhang, J., O'Neill, M. M., Ryken, A., Condon, L. E., & Maxwell, R. M. (2022). A hydrological simulation dataset of the Upper Colorado River Basin from 1983 to 2019. Scientific Data, 9(1), 1–17. https://doi.org/10.1038/s41597-022-01123-w
- Tsai, W. P., Feng, D., Pan, M., Beck, H., Lawson, K., Yang, Y., et al. (2021). From calibration to parameter learning: Harnessing the scaling effects of big data in geoscientific modeling. *Nature Communications*, 12(1), 5988. https://doi.org/10.1038/s41467-021-26107-z
- Vano, J. A., Das, T., & Lettenmaier, D. P. (2012). Hydrologic sensitivities of Colorado River runoff to changes in precipitation and temperature. Journal of Hydrometeorology, 13(3), 932–949. https://doi.org/10.1175/jhm-d-11-069.1
- Verger, A., Baret, F., & Weiss, M. (2013). GEOV2/VGT: Near real time estimation of global biophysical variables from VEGETATION-P data. In MultiTemp 2013: 7th International Workshop on the Analysis of Multi-Temporal Remote Sensing Images (pp. 1–4).
- Verger, A., Baret, F., Weiss, M., Smets, B., Camacho, F., & Lacaze, R. (2014). GEOV2/VGT: Near real time estimation of LAI, FAPAR and cover fraction variables from VEGETATION data within Copernicus Global Land service. In *Fourth International Symposium on recent Advances in Quantitative Remote Sensing*.
- Vertessy, R. A., Watson, F. G., & Sharon, K. O. (2001). Factors determining relations between stand age and catchment water balance in mountain ash forests. Forest Ecology and Management, 143(1–3), 13–26. https://doi.org/10.1016/s0378-1127(00)00501-6
- Wang, H., Huo, X., Duan, Q., Liu, R., & Luo, S. (2023). Uncertainty quantification for the Noah-MP land surface model: A case study in a grassland and sandy soil region. *Journal of Geophysical Research: Atmospheres*, 128(20), e2023JD038556. https://doi.org/10.1029/2023id038556
- Wang, L., Good, S. P., & Caylor, K. K. (2014). Global synthesis of vegetation control on evapotranspiration partitioning. Geophysical Research Letters, 41(19), 6753–6757. https://doi.org/10.1002/2014gl061439
- Wattenbach, M., Franz, D., Liang, W., Schmidt, M., Seitz, F., & Güntner, A. (2012). Integration of MODIS LAI products into the hydrological model WGHM indicate the sensitivity of total water storage simulations to vegetation cover dynamics. In EGU General Assembly Conference Abstracts (p. 10116).
- Webster, C., & Jonas, T. (2018). Influence of canopy shading and snow coverage on effective albedo in a snow-dominated evergreen needleleaf forest. Remote Sensing of Environment, 214, 48–58. https://doi.org/10.1016/j.rse.2018.05.023
- Wei, H., Xia, Y., Mitchell, K. E., & Ek, M. B. (2012). Improvement of Noah land surface model for the warm season processes: Assessment of water and energy flux simulation. *Hydrological Processes*.
- Xia, Y., Mitchell, K., Ek, M., Sheffield, J., Cosgrove, B., Wood, E., et al. (2012). Continental-scale water and energy flux analysis and validation for the North American Land Data Assimilation System project phase 2 (NLDAS-2): 1. Intercomparison and application of model products. *Journal of Geophysical Research*, 117(D3), D03109. https://doi.org/10.1029/2011jd016048

LONGYANG AND ZENG 22 of 23

- Xiao, M., Udall, B., & Lettenmaier, D. P. (2018). On the causes of declining Colorado River streamflows. Water Resources Research, 54(9), 6739–6756. https://doi.org/10.1029/2018wr023153
- Xu, T., Valocchi, A. J., Ye, M., & Liang, F. (2017). Quantifying model structural error: Efficient B ayesian calibration of a regional groundwater flow model using surrogates and a data-driven error model. Water Resources Research, 53(5), 4084–4105. https://doi.org/10.1002/ 2016wr019831
- Yan, K., Park, T., Yan, G., Chen, C., Yang, B., Liu, Z., et al. (2016). Evaluation of MODIS LAI/FPAR product collection 6. Part 1: Consistency and improvements. *Remote Sensing*, 8(5), 359. https://doi.org/10.3390/rs8050359
- Yang, S., Yang, D., & Chen, J. (2019). A machine-learning based surrogate model for distributed hydrological simulation. In AGU Fall Meeting Abstracts (Vol. 2019, pp. H53K–1916).
- Yang, Y., Pan, M., Beck, H. E., Fisher, C. K., Beighley, R. E., Kao, S. C., et al. (2019). In quest of calibration density and consistency in hydrologic modeling: Distributed parameter calibration against streamflow characteristics. Water Resources Research, 55(9), 7784–7803. https://doi.org/10.1029/2018wr024178
- Yin, J., Zhan, X., Zheng, Y., Hain, C. R., Ek, M., Wen, J., et al. (2016). Improving Noah land surface model performance using near real time surface albedo and green vegetation fraction. Agricultural and Forest Meteorology, 218, 171–183. https://doi.org/10.1016/j.agrformet.2015. 12.001
- Yu, K., & D'Odorico, P. (2014). Climate, vegetation, and soil controls on hydraulic redistribution in shallow tree roots. Advances in Water Resources, 66, 70–80. https://doi.org/10.1016/j.advwatres.2014.02.003
- Yuan, W., Zheng, Y., Piao, S., Ciais, P., Lombardozzi, D., Wang, Y., et al. (2019). Increased atmospheric vapor pressure deficit reduces global vegetation growth. Science Advances. 5(8), eaax1396. https://doi.org/10.1126/sciadv.aax1396
- Zahura, F. T., & Goodall, J. L. (2022). Predicting combined tidal and pluvial flood inundation using a machine learning surrogate model. *Journal of Hydrology: Regional Studies*, 41, 101087. https://doi.org/10.1016/j.ejrh.2022.101087
- Zahura, F. T., Goodall, J. L., Sadler, J. M., Shen, Y., Morsy, M. M., & Behl, M. (2020). Training machine learning surrogate models from a high-fidelity physics-based model: Application for real-time street-scale flood prediction in an urban coastal community. Water Resources Research, 56(10), e2019WR027038. https://doi.org/10.1029/2019wr027038
- Zhang, B., Xia, Y., Long, B., Hobbins, M., Zhao, X., Hain, C., et al. (2020). Evaluation and comparison of multiple evapotranspiration data models over the contiguous United States: Implications for the next phase of NLDAS (NLDAS-Testbed) development. Agricultural and Forest Meteorology, 280, 107810. https://doi.org/10.1016/j.agrformet.2019.107810
- Zhang, Y., Gentine, P., Luo, X., Lian, X., Liu, Y., Zhou, S., et al. (2022). Increasing sensitivity of dryland vegetation greenness to precipitation due to rising atmospheric CO<sub>2</sub>. *Nature Communications*, 13(1), 1–9. https://doi.org/10.1038/s41467-022-32631-3
- Zhang, Y., Parazoo, N. C., Williams, A. P., Zhou, S., & Gentine, P. (2020). Large and projected strengthening moisture limitation on end-of-season photosynthesis. Proceedings of the National Academy of Sciences of the United States of America, 117(17), 9216–9222. https://doi.org/10.1073/pnas.1914436117
- Zhang, Y. W., Wang, K. B., Wang, J., Liu, C., & Shangguan, Z. P. (2021). Changes in soil water holding capacity and water availability following vegetation restoration on the Chinese Loess Plateau. Scientific Reports, 11(1), 9692. https://doi.org/10.1038/s41598-021-88914-0
- Zhao, W., Yu, X., Xu, C., Li, S., Wu, G., & Yuan, W. (2022). Dynamic traceability effects of soil moisture on the precipitation-vegetation association in drylands. *Journal of Hydrology*, 615, 128645. https://doi.org/10.1016/j.jhydrol.2022.128645
- Zhu, X., Cai, F., Tian, J., & Williams, T. K. A. (2018). Spatiotemporal fusion of multisource remote sensing data: Literature survey, taxonomy, principles, applications, and future directions. *Remote Sensing*, 10(4), 527. https://doi.org/10.3390/rs10040527
- Zhu, Z., Bi, J., Pan, Y., Ganguly, S., Anav, A., Xu, L., et al. (2013). Global data sets of vegetation leaf area index (LAI) 3g and fraction of photosynthetically active radiation (FPAR) 3g derived from global inventory modeling and mapping studies (GIMMS) normalized difference vegetation index (NDVI3g) for the period 1981 to 2011. Remote Sensing, 5(2), 927–948. https://doi.org/10.3390/rs5020927

LONGYANG AND ZENG 23 of 23